Field Ion Microscopy for the Characterization of Scanning Probes

5

William Paul and Peter Grütter

Contents

1 Definition of the Topic ... 160
2 Overview ... 160
3 Field Ion Microscopy for the Characterization of Scanning Probes ... 161
3.1 Introduction ... 161
3.2 Experimental and Instrumental Methodology ... 164
3.3 Key Research Findings ... 182
3.4 Conclusions and Future Perspective ... 192
References ... 193

Abstract

Scanning probe microscopy (SPM) is a widely used tool for investigating the nanoscale structure of materials, as well as their electronic and mechanical properties with its related spectroscopic modes of operation. In SPM experiments, the sharp tip which probes the material under investigation is usually uncharacterized; however, its geometry and chemical composition play a large role in the SPM's lateral imaging resolution and the features recorded in electronic and force spectroscopies. To carry out comparisons with modeling, one must consider a set of plausible tip structures and choose the one which best reproduces the experimental data recorded with the uncharacterized tip.

With an atomically defined tip prepared by FIM, the electronic and mechanical properties of the SPM probe are predetermined before the experiment, permitting

W. Paul (✉)
IBM Research Division, Almaden Research Center, San Jose, CA, USA
e-mail: wmppaul@gmail.com

P. Grütter
Physics Department, McGill University, Montréal, QC, Canada

© Springer-Verlag Berlin Heidelberg 2015

C.S.S.R. Kumar (ed.), *Surface Science Tools for Nanomaterials Characterization*,
DOI 10.1007/978-3-662-44551-8_5

direct comparison with theory, as well as the quantitative determination of parameters which depend on tip radius, such as stresses during indentation.

Here we describe the implementation of FIM for the characterization of scanning probe apices. This includes topics of tip integrity, characterization, advanced preparation methodologies, and key research findings from experiments which combine FIM and SPM techniques.

Keywords

Field ion microscopy (FIM) • Scanning probe microscopy (SPM) • Scanning tunneling microscopy (STM) • Atomic force microscopy (AFM) • Field emission • Single-atom tips • Tip characterization • Nanoelectronics • Nanomechanics

1 Definition of the Topic

The field ion microscope (FIM) can image the atomic structure of sharp metal tips with nanometer-sized radii and is notable as being the earliest technique to produce atomically resolved images of matter in real space. Using FIM, one can atomically characterize, and even engineer, the sharp tips used in scanning probe microscopy (SPM). In this chapter, we address the technical aspects of implementing these tips in SPM experiments and review their application to scanning tunneling microscopy (STM), atomic force microscopy (AFM), and SPM-based nanoindentation experiments.

2 Overview

Scanning probe microscopy (SPM) is a widely used tool for investigating the nanoscale structure of materials, as well as their electronic and mechanical properties with its related spectroscopic modes of operation. In SPM experiments, the sharp tip which probes the material under investigation is usually uncharacterized; however, its geometry and chemical composition play a large role in the SPM's lateral imaging resolution and the features recorded in electronic and force spectroscopies. To carry out comparisons with modeling, one must consider a set of plausible tip structures and choose the one which best reproduces the experimental data recorded with the uncharacterized tip.

With an atomically defined tip prepared by FIM, the electronic and mechanical properties of the SPM probe are predetermined before the experiment, permitting direct comparison with theory, as well as the quantitative determination of parameters which depend on tip radius, such as stresses during indentation.

Here we describe the implementation of FIM for the characterization of scanning probe apices. This includes topics of tip integrity, characterization, advanced preparation methodologies, and key research findings from experiments which combine FIM and SPM techniques.

3 Field Ion Microscopy for the Characterization of Scanning Probes

3.1 Introduction

The utility of the FIM for preparing and characterizing tips destined for SPM experiments was considered by Hans-Werner Fink of IBM Zürich in the context of STM shortly after its invention [1]. The main advantage of an atomically defined tip apex is that if the exact atomic arrangement of the apex is known, the electronic structure of the tip and the lateral resolution of the STM are predetermined. The same detailed knowledge of the apex termination, as well as the tip radius, is useful for atomic force microscopy (AFM) experiments and important in the interpretation of results from combined STM and AFM experiments.

Largely unknown, the atomic-scale tip structure is directly responsible for image contrast [2, 3], as well as the details of the measured electronic properties by scanning tunneling spectroscopy [4, 5], chemical bonding forces by force spectroscopy [6, 7], and yield point of materials by indentation [8, 9]. In order to obtain quantitative and reproducible data, which could be considered as a benchmark for computational simulations, one requires a tip with known atomic structure. For example, FIM-characterized tips could act as atomically defined electrodes to build junctions to single molecules, where transport properties are sensitive to the atomic arrangement of the contact electrodes [10].

One must first sort out the technical challenges surrounding the experiment, starting with the reliable transfer of an atomically defined FIM tip to an SPM experiment: this involves moving the tip and sample from an initial separation of the order of meters to a working distance of some angstroms in a brief period of time and without crashing one into the other. Many questions need to be addressed concerning the implementation of FIM tips in SPM: Will the atomically defined tip be modified by impurities in the FIM imaging gas? If so, can this be avoided? Although UHV is very clean, it still has a finite rest gas pressure – how long will the atomically defined tip remain atomically defined in vacuum? How much time do we have to perform our atomically defined SPM experiment? How can we approach the tip to the sample and ensure that it doesn't crash or become modified upon interaction with the substrate?

This chapter begins with a brief introduction to FIM and SPM, and then in Sect. 3.2, we focus on the experimental methodologies of FIM which are most relevant to the characterization of SPM tips. Section 3.3 reviews research findings from STM, AFM, and nanoindentation experiments with atomically defined probes.

3.1.1 Field Ion Microscopy (FIM)

The field ion microscope was invented in 1951 by Erwin W. Müller [11] and by 1956 had achieved the first real-space images of matter with atomic resolution. The first FIM images were of the atomic arrangement of the apex of very sharp tungsten needles. By 1957, the surfaces of other refractory metals had also been imaged [12]. Although the atomic resolution of FIM is no longer unique among microscopes

(TEM, SEM, STM, and AFM have all demonstrated atomic spatial resolution), there still exist distinctive experimental applications of FIM. Particularly well suited to FIM is the study of diffusion of single atoms or clusters on crystal surfaces, and this technique has generated most of the existing experimental data about the diffusion of atoms and clusters on metal surfaces [13].

Another unique feature of the FIM is the possibility of integrating a time-of-flight (ToF) mass spectrometer to enable chemical analysis with single-atom sensitivity and a spatial resolution of several angstroms. The combined technique is known as atom probe field ion microscopy (AP-FIM) or more simply as the atom probe [14–17]. In AP-FIM, a pulsed field is applied to the FIM specimen to field evaporate a small amount of material from its surface to be chemically analyzed in the ToF unit; it is a destructive technique, consuming the sample as data is collected. Tien T. Tsong, a colleague of Müller's from the beginning of FIM, wrote in his book on AP-FIM [12] that the technique provides the "ultimate sensitivity in chemical analysis" because of its exquisite single-atom sensitivity.[1] Unlike scanning probe methods, AP-FIM can access the chemical composition in the bulk of samples, and technique development remains very active today in the computational reconstruction of the data into 3D element-specific atomic maps. Applications of AP-FIM include the investigation of chemical segregation of elements at crystalline defects (steels and semiconductors), local studies of grain boundaries in nanocrystalline materials (with grains too small for techniques like electron backscatter diffraction (EBSD) [20]), and short-range order in materials (e.g., in high-temperature superconductors).

3.1.2 Scanning Probe Microscopy

Scanning probe microscopy uses a physical probe to image surfaces by raster scanning the surface and monitoring some type of interaction between the probe's apex and the sample. In STM, a small current tunneling between the tip and the sample, on the order of pA to nA, is used as an imaging mechanism [21–23]. Due to the current's exponential dependence on the tip-sample distance, with one decade of variation per angstrom, excellent spatial resolution is possible. In AFM, the force or force gradient between the tip and sample is responsible for image contrast [24, 25]. Electrostatic, van der Waals, and chemical bonding forces all contribute to the force-distance profile, so the AFM's resolution depends on which particular force interaction is dominant.

STM and AFM are usually operated under feedback to maintain either constant current or force (or force gradient) while the tip scans the surface. This procedure traces out an isosurface of constant tip-sample interaction, often termed the "topography" of the sample. In particularly stable instruments, often at cryogenic

[1] We note that single-atom chemical sensitivity has also been achieved recently in STM and AFM techniques: inelastic electron tunneling spectroscopy in STM allows for measurement of the vibrational energies of individual chemical bonds, which is a form of chemical sensitivity – for example one can distinguish between hydrogen and deuterium bonds [18, 19]. In the case of AFM, however, it is more of a *relative* chemical sensitivity obtained by comparing force-distance interaction curves from different atomic species with the same tip. Absolute chemical identification relies on the specifics of the tip apex which is usually unknown [6].

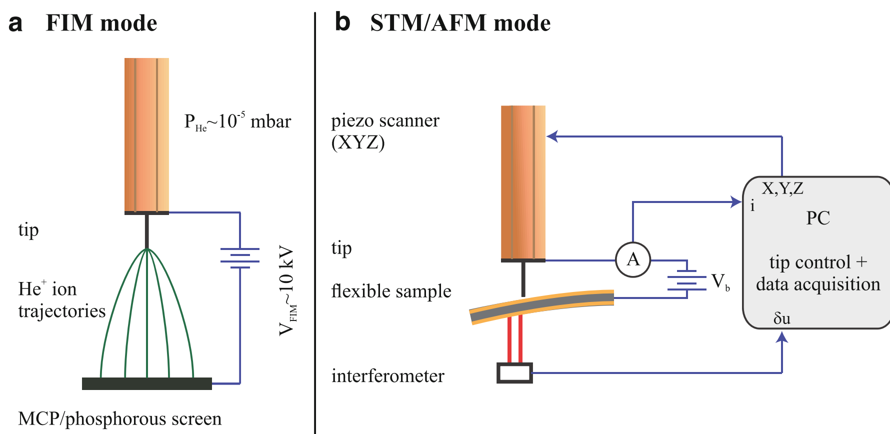

Fig. 5.1 Schematic of the microscope's two principle modes of operation: (**a**) FIM mode; (**b**) STM/AFM mode

temperatures, a constant height scan over the sample can be performed while the variations of current or force are recorded as a function of tip position, forming an "image" of these interactions. SPM can also be used to perform spectroscopy, in which one parameter is modified and the response of another is measured, such as force versus distance, current versus voltage, etc.

In all SPM experiments, the tip structure has a crucial role in contrast formation and data interpretation. Surface science has progressed to the point where the SPM community is able to study exquisitely well-defined surfaces, but the tip of the SPM remains mostly uncharacterized – often one must turn to atomistic modeling to guess at possible structures [7, 26]. Exceedingly few SPMs exist with in situ tip characterization facilities – in this chapter, we consider FIM as a characterization tool for the sharp SPM tips.

3.1.3 Combined STM/AFM/FIM

As an example of an apparatus which combines STM, AFM, and FIM, we describe the system used in our group's experiments [27–29]. The combined STM/AFM/FIM is operated in two modes illustrated in Fig. 5.1. In FIM mode, the apex of the sharp tip is imaged with atomic resolution. As illustrated in Fig. 5.1a, the measurement chamber is backfilled with He gas to $\sim 10^{-5}$ mbar, and a high positive voltage of $\sim$10 kV is applied to the tip. The ionized He gas atoms, reporting on the atomic arrangement of the tip apex, are detected by a microchannel plate (MCP) and phosphor screen.

In the STM/AFM mode shown schematically in Fig. 5.1b, a cantilevered sample is placed under the tip.[2] The tip is approached to tunneling interaction under applied

[2]An unconventional setup which allows tungsten probes, compatible with the high electric fields in FIM, to be used as SPM tips. The development of new AFM force sensors such as the qPlus [30] and length extension resonator [31, 32] conveniently allow tungsten probes to be used for AFM.

bias V_B, while current I is measured by an ammeter [33]. A computer monitors the current and regulates the tip height with the piezo tube actuator to maintain a constant current. Meanwhile, a dual-beam interferometer is used to record the deflection of the cantilevered samples [34], which permits the measurement of forces acting in the tip-sample junction.

3.2 Experimental and Instrumental Methodology

3.2.1 Operating Principle of the FIM

FIM is a particularly simple microscopy technique in comparison to the complexities of electron optics in SEM and TEM, or the control systems and vibration isolation required for SPMs. In its most basic implementation, FIM requires a sample in the shape of a sharp tip, a phosphor screen at a distance of $\sim$10 cm from the tip, a vacuum system backfilled with $\sim 10^{-5}$ mbar of He, and a high voltage supply.

In FIM, a high positive voltage is applied to the tip, and when the electric field approaches $\sim$4 V/Å at the tip, He gas atoms will be ionized and accelerated toward the screen. The ionization of He atoms occurs with the highest rate near surface sites on the tip where the electric field is largest: the field is locally enhanced in positions of reduced radius of curvature such as at atoms located at the edges of atomic planes, individual atoms adsorbed in the middle of atomic planes, and over atoms contained in highly corrugated planes (such as the W(111) plane). The image which forms on the phosphor screen reflects the spatial distribution of the He ionization rate and thus gives atomically resolved information regarding the tip shape.

It is important to point out that the specimen must be shaped like a needle with a very sharp apex in order to achieve a sufficient geometric enhancement of the electric field at its apex.[3] Another important consideration in dealing with such high electric fields is that not all materials can withstand such fields. The destruction of the tip under the applied field can be avoided to some extent by cooling the tip to low temperatures in order to inhibit thermally activated field desorption. Another strategy for imaging softer materials is to employ a different imaging gas such as Ar or Ne which ionizes at lower electric fields, 2.2 and 3.75 V/Å, respectively, compared to 4.4 V/Å for He [10]. Tungsten is the only metal which can withstand room temperature He ion FIM without field evaporating during imaging. Iridium tips, for example, cannot be imaged by He ion FIM at room temperature, but can withstand the fields required to form a Ne ion FIM image [35].

The process of field ionization is illustrated in Fig. 5.2. The dipole attraction of gas atoms occurs near the apex in the presence of the strong field. If the tip is cooled, the gas atoms will thermalize to the tip as they hop over its surface – this contributes to a lower initial random thermal velocity when the gas atom ionizes and helps improve lateral spatial resolution (Sect. 3.2.2). The He gas atom has the highest probability of

[3] These fields are the highest achievable by laboratory techniques and are comparable in magnitude to those inside ionic crystals [10].

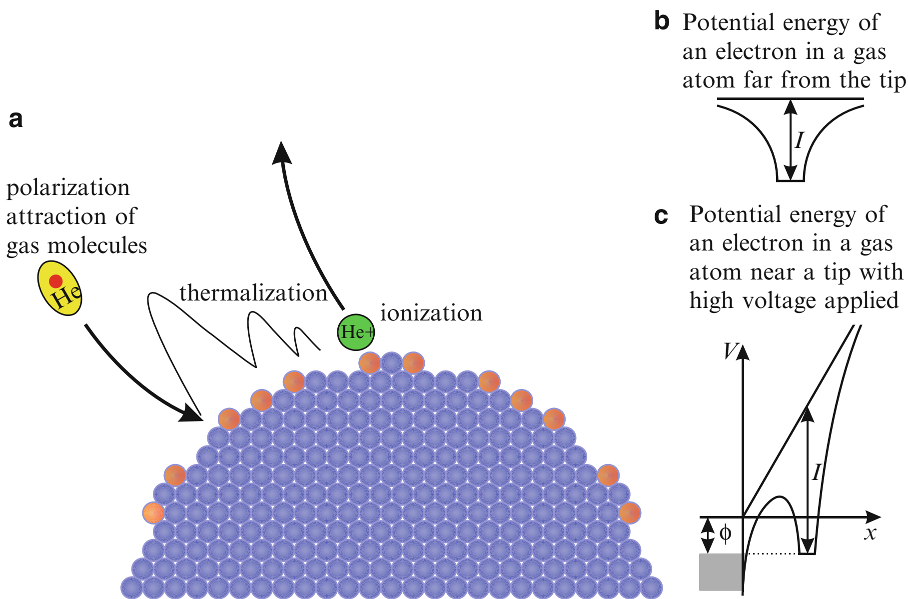

Fig. 5.2 (**a**) Side view of a tip apex showing schematically the dipole attraction of imaging gas atoms, thermal accommodation to the tip, and ionization over an atomic site of locally enhanced field (*orange*). (**b**) Potential energy diagram of a valence electron in a gas atom. (**c**) Potential energy diagram when the atom is within tunneling distance of the metal tip and in a large electric field

being ionized over a protruding atom where the field is locally enhanced, such as those indicated in orange. Once ionized, the He^+ ion is accelerated by the field toward a microchannel plate and phosphor screen for detection.

The loss of an electron from the gas atom to the tip happens by quantum mechanical tunneling. The potential energy landscape of a valence electron in a gas atom with ionization energy I is shown in Fig. 5.2b. In an applied field, the potential becomes sloped. When brought sufficiently close to a metal tip, as illustrated by Fig. 5.2c, the barrier between the electron state in the gas atom and an available electron state in the tip becomes small enough to tunnel through. Applying the WKB method to an equilateral triangle potential well, it is possible to calculate the barrier penetration probability at the critical distance of field ionization as [12]

$$D(F) = \exp\left\{-\left(\frac{8m}{\hbar^2}\right)^{\frac{1}{2}}\frac{2}{3}\left(I - 2\sqrt{e^3F}\right)^{\frac{1}{2}}\frac{I-\phi}{F}\right\}, \tag{5.1}$$

where m is the free electron mass, $\hbar$ is the reduced Planck's constant, e is the elementary charge, I is the ionization energy of the gas atom, F is the magnitude of the applied electric field, and φ is the work function of the tip. It is clear from the illustration of the barrier in Fig. 5.2c and by the result of Eq. 5.1 that the tunneling rate is strongly dependent on the ionization energy of the gas itself (increases with

decreasing ionization energy), as well as the magnitude of the applied field (increases with increasing applied field).

3.2.2 Spatial Resolution of the FIM

The excellent spatial resolution of the FIM allows us to resolve individual atoms on the W(111) plane, where the tip is sufficiently corrugated so that substantial variations in the electric field occur over the surface. We are often asked how it is possible to obtain atomic resolution images of tips at room temperature since most implementations of FIM are cryogenic – at least at liquid nitrogen temperatures, if not below. The answer has two components: Firstly, the extraordinary sharpness of our tips, compared to most used in traditional FIM, enhances the microscope's resolution. Secondly, low temperature, while necessary for studying the diffusion of adsorbed atoms (used to "freeze" their position on the tip's surface during high-field imaging), is not required for characterizing a stable tungsten tip.

We will now discuss the origins of the spatial resolution and show that for tips with sufficiently small radii, the expected spatial resolution is adequate for atomic resolution imaging. In the imaging process, helium atoms are ionized over specific sites on the tip – we consider what effects will broaden the projection of these ionization sites when the helium ions are visualized on the screen. Three factors affect this resolution [12]: the ionization disk size, Heisenberg's uncertainty principle, and thermal broadening. Since these effects are statistically uncorrelated, they are added in quadrature to give the total resolution broadening as a quadrature sum of the components listed above (in order):

$$\delta = \sqrt{\delta_0^2 + \delta_u^2 + \delta_T^2}. \tag{5.2}$$

The ionization disk size reflects an intrinsic diameter of the ionization zone above each surface atom and is approximated to be a constant on the order of $\delta_0 = 2.5$ Å [36]. The subsequent terms in Eq. 5.2 contribute to a broadening beyond this baseline resolution. The second term considers the Heisenberg uncertainty contribution on the tangential velocity component of the gas atom when it is ionized:

$$\delta_u = 2\left(\frac{\beta^2 r_t \hbar^2}{2kem_{\mathrm{gas}}F_0}\right)^{\frac{1}{4}}. \tag{5.3}$$

In the above equation, β is a geometric factor taking into account image compression due to the fact that the tip is not a perfect hemisphere but has a shank. β is on the order of 1.5–1.8 [12] and is taken to be 1.65 in the following calculation. r_t is the tip radius, k is a geometric field reduction factor of $\sim$6 (depends on tip shape, usually $3 < k < 8$ [37]), m_{gas} is the atomic mass of the imaging gas, and F_0 is the magnitude of the ionizing electric field.

The last term represents the broadening due to the initial thermal velocity of the imaging gas atoms:

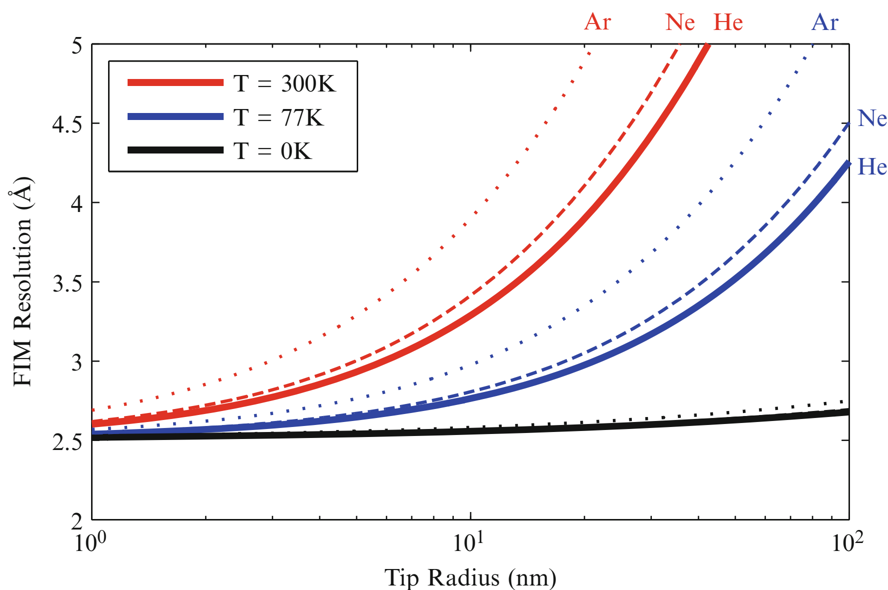

Fig. 5.3 Resolution of FIM as a function of tip radius at room temperature, liquid nitrogen temperature, and absolute zero. Curves for ionization fields corresponding to He, Ne, and Ar imaging gases are shown as *solid*, *dashed*, and *dotted lines*

$$\delta_T = 4\left(\frac{\beta^2 k_B T r_t}{K e F_0}\right)^{\frac{1}{2}}, \tag{5.4}$$

where k_B is the Boltzmann constant and T is the temperature of the gas atom; the other variables have been described previously.

The parameters over which one has practical experimental control are temperature, tip radius, and species of imaging gas. The choice of imaging gas affects the mass term in Heisenberg broadening, Eq. 5.3, but this is generally outweighed by the modification of best imaging field which enters more strongly into Eq. 5.4 for thermal broadening ($F_0 = 4.4$, 3.7, 2.2 V/Å for He, Ne, and Ar, respectively). The combined resolution of FIM, given by Eqs. 5.2, 5.3, and 5.4, is plotted in Fig. 5.3 as a function of tip radius. Temperatures of 300, 77, and 0 K are shown in red, blue, and black, respectively. For each temperature, the resolution achieved by He, Ne, and Ar is indicated by solid, dashed, and dotted lines. Our FIM tip radii mostly fall in the range of 3–12 nm, where for room temperature (and below), the resolution is sufficient to image atoms on the W(111) plane spaced by ~4.5 Å. Larger tips in the range of tens to hundreds of nanometers clearly require low temperatures to achieve atomic resolution.

A last comment on resolution is that the preceding discussion applies to the smallest distance between surface atoms that can be resolved in an image. However, when an adatom is deposited on a surface for diffusion studies in FIM, one can fit

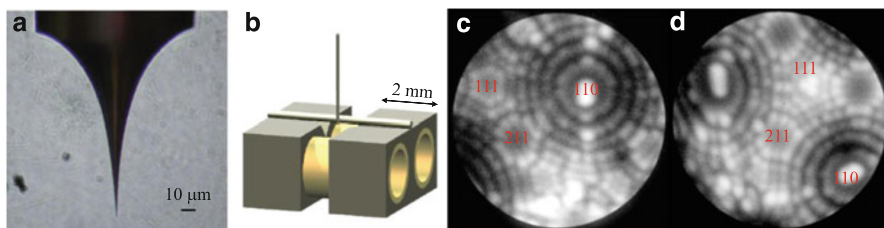

Fig. 5.4 (**a**) Optical microscope image of an electrochemically etched 0.125 mm diameter tungsten wire; (**b**) tip holder design; (**c**) W(110) tip with a radius of 9.4 ± 0.8 nm; (**d**) W(111) tip with a radius of 9.6 ± 0.7 nm

the image intensity distribution and locate its centroid to ~0.3 Å [12]. Another important effect that doesn't enter into the resolution equation is the selective imaging of atoms where the electric field is enhanced by local corrugation and the suppression of imaging on large flat planes of atoms. On smooth, densely packed planes such as the W(110), FIM resolution is effectively nonexistent because surface atoms are not imaged.

3.2.3 Tip Etching and Preparation

Tungsten tips for FIM and SPM experiments are etched in a 9.8 M KOH solution by electrochemical etching at 3 V_{DC}, along the lines of standard procedures found in the STM literature [38–40]. The procedure and design of an electrochemical bath was recently reported by our group [41], and very detailed accounts related to tip preparation can be found in the PhD thesis of Till Hagedorn [28] and the MSc work of Anne-Sophie Lucier [37, 42]. In this section, we will focus on tungsten tips because of the simplicity with which they can be fabricated and imaged in room temperature FIM. For an account of etching iridium tips for FIM/SPM in $CaCl_2$, we refer the reader to Ref. [35].

The typical concave shape of tungsten STM tips is shown in an optical microscope image in Fig. 5.4a. This shape forms automatically during the etching process, having to do with the meniscus shape and currents in the etching solution around the tip shank. Routine success in creating sharp tips during etching is mostly dependent on obtaining a meniscus around the wire which is undisturbed by vibrations, bubbles, or debris in the etching solution and a reliable electronic circuit which removes the applied bias when a sudden drop in electrochemical current is detected.

The etched tips are transferred to UHV and are annealed to an orange glow to remove the tungsten oxide layer and any physisorbed gas on their surfaces. The tip holder design, shown in Fig. 5.4b, is particularly well suited for heating and degassing the entire tip wire. The tungsten tip wire is spot welded to a 0.25 mm diameter annealed 304 stainless steel wire (Alfa Aesar), which is in turn spot welded to the two electrically isolated halves of the tip holder. The stainless steel wire acts as a filament to resistively heat and degas the entire tungsten wire. Mounting tips to a filament is common in conventional FIM, implemented not

only to clean the tips but also in order to rapidly warm them momentarily from cryogenic temperatures to study diffusion of adatoms on their surfaces [12, 13].

After annealing, tips are field emitted against a copper anode placed several mm from their apices. The voltage at which field emission occurs gives a good indication of their sharpness. Since electron emission necessitates a field of ~5 V/nm and ionization of helium gas requires ~5 V/Å, when an appreciable field emission current (~100 nA) is observed at an applied voltage of <1 kV, one can be confident that the tip is sufficiently sharp that an ion image can be obtained in FIM at an applied voltage of <10 kV (the limit of our high voltage supply). Our experience with field emission indicates sensitivity to the placement of the anode electrode and the geometric details of mounting the tip to the holder (long or short tip wire) – these observations are supported and explained by a recent paper by Setvín et al. [43]. We therefore only use field emission as a rough guide to tip sharpness.

Tungsten tips with (110) and (111) apex orientations are commonly used in our studies. W(110) tips result from etching 0.1 mm diameter polycrystalline wire (Alfa Aesar). Polycrystalline tungsten wire is highly textured from the cold drawing process and consists of long and thin ~1 × 50 μm grains oriented in the (110) direction to within a few degrees of its axis [44]. This strong crystallographic texture is common to all cold drawn bcc metals [45]. For our tips having typical apex radii of a few nm, the relevant part of the "polycrystalline" tip is effectively a single crystal. W(111) tips are etched from 0.125 mm diameter single crystal wire oriented to within 2° of the axis (Applied Physics Technologies).

FIM images of W(110) and W(111) tips are presented in Fig. 5.4c, d, respectively. Low-index crystal planes are identified in the micrographs. The planes can be visually identified by their symmetry (twofold or threefold in these cases), their relative size, and placement with respect to each other. Stereographic projection maps, such as the one published in Fig. 3.6 of Ref. [12], are helpful to identify the planes with respect to each other. The radii of the tips shown in Fig. 5.4 are 9.4 ± 0.8 nm and 9.6 ± 0.7 nm, respectively, as determined by averaging results from ring counting between all visible (110), (211), and (111) planes. The gray scale images were created using the green channel (the phosphor screen glows green) of an RGB image obtained by averaging many individual photographs. Image contrast is adjusted using a logarithmic curve to help bring out features which are not otherwise visible in the dynamic range of print or computer displays. This processing technique lends our FIM data a remarkably high printed quality.

3.2.4 Radius Determination by Ring Counting

The most straightforward way to determine the radius of an FIM tip is to use the "ring counting" method [12, 37, 46]. With the assumption that the apex of the tip has spherical envelope, one can count the number of atomic steps between crystallographic planes, which show up as "rings" in the FIM micrograph, and determine the radius by simple geometry (to follow). A spherical envelope is a good approximation within the region of the tip in which we are interested – ball models of tips created by cutting a bcc crystal in a hemisphere give good correspondence to the features seen in FIM images. It is worth noting that more elaborate techniques have

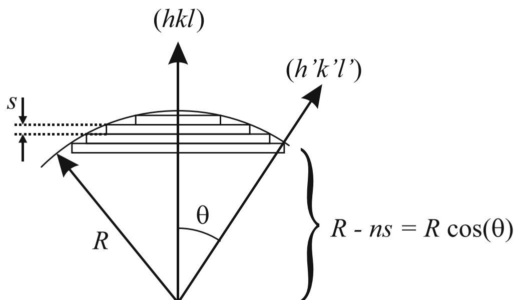

Fig. 5.5 FIM tip apex with radius R showing geometry for ring counting. Planes of interlayer spacing s are normal to direction *(hkl),* and n rings are counted between poles *(hkl)* and $(h'k'l')$. The angle between these poles is θ

been developed to extract the surface profile of FIM tips from features in micrographs [47, 48], essentially by using ring counting between various crystallographic poles to extract Cartesian (x, y, z) coordinates of the surface atoms. These are particularly useful if one is interested in determining the cross-sectional profile out into the far edges of the FIM image (which in our case is blocked by an aperture).

The ring counting method can be described as follows [12]: Assuming a spherical envelope of the tip apex, the local radius of curvature, R, between two crystallographic poles separated by angle θ can be found by counting the number of visible rings, n, between them. Using the interlayer spacing, s, corresponding to the appropriate crystal plane, the local radius of curvature is given by

$$R = \frac{ns_{(hkl)}}{1 - \cos\theta}. \tag{5.5}$$

This equation describes the geometry illustrated in Fig. 5.5.

For the ring counting estimations to be accurate, each counted ring must correspond to a *single* atomic step of type *(hkl).* We will soon demonstrate that in FIM micrographs, a single "ring" can correspond to multiple atomic planes of height s – counting rings is not equivalent to counting steps. The underestimation of FIM tip radii can occur when the rings appearing in the micrograph correspond to *more than one* atomic plane. The standard description of ring counting could be more precisely expressed in the following way: assuming a spherical envelope of the tip apex, the local radius of curvature is determined by counting the number of steps, n, of height s between crystallographic poles with angle θ between them.

The ring counting method can be applied to different choices of *(hkl)* pole, but the rings of the (110) plane are the most straightforward to identify because they have the largest step height in the bcc crystal. The (110) plane also happens to be the apex of most polycrystalline tungsten tips as a consequence of the wire's manufacturing by cold drawing [44].

In Fig. 5.6, we present ball models of tungsten tip apices of radii 3.0, 4.7, 6.0, and 9.0 nm. The models were created by carving a hemispherical shell from a bcc crystal with a (110) apex. The atoms in the outermost 0.05 nm shell are shaded lighter in

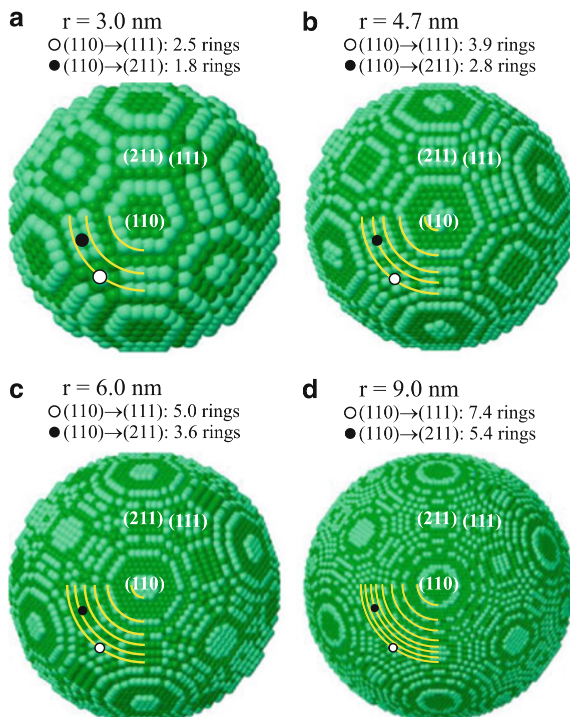

Fig. 5.6 Top view (looking toward the apex) of ball models of W(110) tips with radii (**a**) 3.0 nm, (**b**) 4.7 nm, (**c**) 6.0 nm, and (**d**) 9.0 nm. Quarter-circle lines highlight the (110) rings at step edges. The center of the (111) and (211) poles are indicated by *white* and *black circles*, respectively

order to highlight the atoms at terrace edges which would be imaged brightly in FIM (a common method of visualizing atomic geometry with ball models [49, 50]).

As the tip radius increases, the size of crystallographic facets increases – for example, the (211) facet has just two rows of atoms in Fig. 5.6a but has five rows of atoms in Fig. 5.6c. Correspondingly, the number of rings increases between the centers of crystallographic poles. From Eq. 5.1, we have calculated the expected number of rings n between the (110) apex and the (111) and (211) poles, indicated in Fig. 5.6 with corresponding white and black circles. The centers of these planes are indicated by circles on the ball models.

The expected number of rings corresponds well with the number of rings counted from the tip apex to the center of the crystallographic poles (the rings are indicated by concentric quarter circle lines at the edge of the (110) steps). The number of rings can be thought of as the number of (110) steps that must be descended from the (110) apex in order to reach the center of the $(h'k'l')$ pole in question. For these tips of relatively small radii and for the small angles between the apex and the (111) and (211) directions, there is a single (110) plane for each ring; therefore, the estimation of ring counting is accurate.

Comparing the calculated number of rings to the rings visible in the ball models, it is apparent that a better estimation of the tip radius is obtained using a count of n–1 instead of n: this off-by-one error can be explained in Fig. 5.5 where it is the

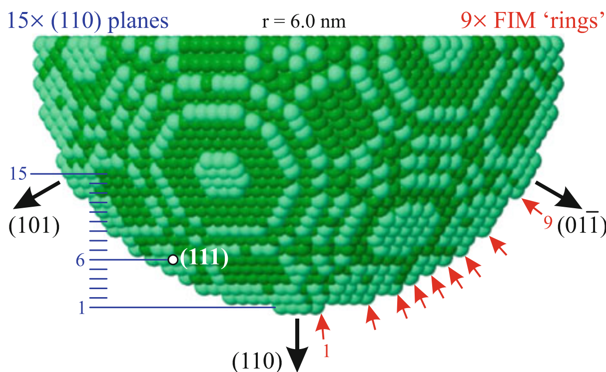

Fig. 5.7 Side view of the 6.0 nm radius W(110) tip presented in Fig. 5.6c. There are 15 layers of (110) planes between the apex and the (101) facet (*dark blue lines*), but only 9 "rings" apparent in the micrograph (*red arrows*). The estimation based on 14 × 0.446 nm yields a radius of 6.2 nm, whereas 9 × 0.446 nm yields an underestimated radius of 4.0 nm. The (111) apex is shown at layer #6 from the (110) apex. The angle between (110) and (111) is sufficiently small that the number of rings corresponds exactly to the number of (110) steps

number of steps crossed to get from *(hkl)* to $(h'k'l')$ that matters (one less than the total number of rings). This is usually a small correction but becomes increasingly important with decreasing tip radius. This concern is equivalently expressed by starting to count rings at 0 rather than 1, as done by Webber [46].

The first serious error that can occur in ring counting consists of counting FIM rings which correspond to more than one atomic plane of type *(hkl)*. This becomes problematic when rings are counted between planes of large angular separation (e.g., (110) type planes that are 60° apart [51]). Shown in Fig. 5.7 is the side view of the 6.0 nm tip presented in Fig. 5.6c. Counting the rings between (110) and $\left(01\bar{1}\right)$ yields nine rings, indicated by red arrows on the right half of the image. As the angle from the apex increases, the visible rings begin to correspond to more than one (110) plane. This is illustrated by the blue "ruler" on the left half of the image where we have counted 15 atomic planes between the (110) apex and the center of the (101) plane. Using $n = 9$, we obtain a radius of 4.0 nm, whereas a more accurate estimate is obtained using $n–1 = 14$, yielding a radius of 6.2 nm.

A second common ring counting error arises from the use of the wrong interlayer spacing. The interlayer spacing s must correspond to that of the *(hkl)* pole – the initial pole – not $(h'k'l')$, the final pole. Using the (111) plane spacing rather than (110), Urban et al. [52] deduced a tip radius of 14.4 nm, whereas we estimate a radius of the order ~32 nm by counting ~21 rings from (110) to (211). These problems are again seen in Pitters et al. [53] where the 3 and 5 nm radii tips determined by the authors are actually of the order 6 and 10 nm, and also in Rezeq et al. [54] where the 1.4 nm radius apex should be ~4.8 nm (although the image resolution makes the identification of (110) and (111) planes difficult).

To summarize, the key elements to proper radius determination by ring counting are as follows:

- n must be accurately determined – its value must correspond to the number *single* steps of type s.
- s must correspond the plane spacing of (hkl), not $(h'k'l')$.
- n should be replaced by n–1 for a more accurate radius estimation for small tips (or equivalently, counting should begin at zero)

We also urge the use of (110) planes for ring counting due to their large step height and not (111): rings corresponding to single (111) steps are very difficult to discern because of the small (111) step height. The routine construction of ball models of FIM tips also helps to familiarize the experimenter with the appearance of tips with different radii.

Finally, to quickly estimate a tungsten tip radius in nm, one can simply multiply the number of rings from (110) to (211) by 1.66 nm · ring^{-1} or multiply the number of rings from (110) to (111) by 1.21 nm · ring^{-1} (these factors are $s_{(110)}/(1–\cos\theta)$).

3.2.5 Advanced Tip Preparation: Etching and Faceting

In this section, we mention other tip preparation techniques beyond the standard procedure of tungsten tip etching and FIM characterization. Gas etching and tip faceting are well established in the FIM community and offer exciting opportunities to atomically engineer the apices of SPM tips.

The sharpening of tips using nitrogen gas is rather straightforward and has been well studied in the context of building sharp tips for field ion emission in helium ion microscopes or electron emission for coherent electron sources and point projection microscopes. The nitrogen sharpening process was first reported by Rezeq et al. [54] and patented by the same authors in 2008 [55].

The process occurs by adsorption of nitrogen on the tungsten tip shank, illustrated in Fig. 5.8. The nitrogen cannot bind to the very apex of the tip because the electric field there is too large – the gas is ionized and repelled before it can reach the tip surface. Nitrogen can, however, bind to the shank of the tip where the field is not as high. This happens by dissociative adsorption in which a single nitrogen atom forms a chemical bond to a tungsten atom on the tip's surface (this reaction is discussed in Sect. 3.2.6 and is addressed specifically in Refs. [56, 57]). The W-N bond weakens the W atom's bond to its neighbors and lowers the field necessary to evaporate the W-N complex, shown schematically in the patent illustration reproduced in Fig. 5.8a, b.

The weakened tungsten atoms are thus preferentially etched by field evaporation from the tip shank. The resulting reduction in the local radius of curvature of the tip apex is illustrated in Fig. 5.8c. The final profile of the tip is somewhat different than the original: a shoulder is formed where the field on the shank is no longer strong enough to evaporate the W-N (this shape has been experimentally verified by SEM in Ref. [52]). At its apex, the radius is much reduced and can be etched to terminate in a single atom.

One distinct advantage of this tip sharpening technique is that it can be monitored by helium ion FIM imaging during the etching process. Figure 5.9a–e shows a sequence of FIM images during nitrogen sharpening of a W(111) tip at room temperature, beginning at a radius of ~4.3 nm and ending with a radius of ~2.5 nm

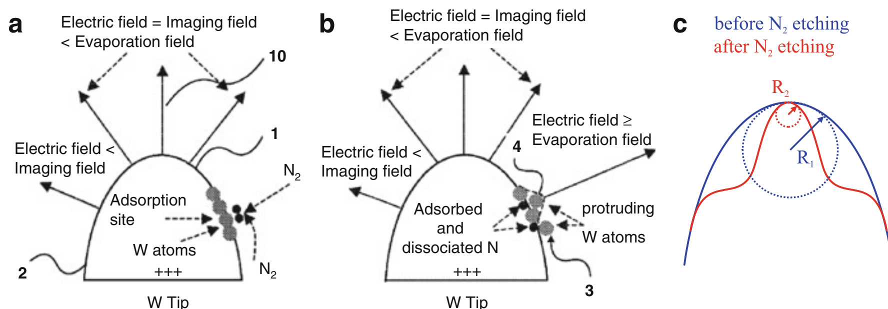

Fig. 5.8 Schematic description of the sharpening process. (**a**) N_2 can only adsorb to the tip shank where the field is lower than at the apex. (**b**) The W-N bond weakens the bonding of the W atoms to the tip, and they field evaporate, leading to a preferential loss of material around the tip shank. (**a**) and (**b**) public domain illustration from Ref. [55]. (**c**) Tip profile before etching (*blue*), and after (*red*), illustrating a reduction in local radius of curvature at the apex and the final "shouldered" shape of the tip

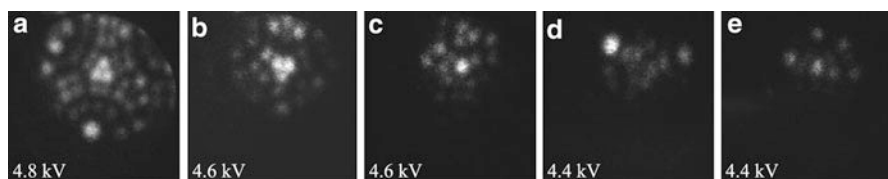

Fig. 5.9 (**a**–**e**) Sequence of FIM images during nitrogen etching at 5×10^{-7} Torr N_2, constant pressure

by image (d). The applied voltage was reduced as necessary to slow evaporation of the tip apex atoms while the apex radius decreased. In this experiment, the nitrogen pressure was constant at 5×10^{-7} Torr. The atomic geometry of the apex could not be completely stabilized due to the nonadjustable nitrogen pressure and the lack of cryogenic cooling during this experiment. However, it demonstrates the impressive efficiency of the technique.

Nitrogen etching may serve as a useful technique to produce tips of varying radii for nanomechanics studies; however, the uncharacterizable shape of the tip shoulder (Fig. 5.8c) could present difficulties in predicting the mechanical properties of the apex. The technique is certainly applicable to experiments with atomically defined SPM junctions provided that single-atom tips can be stabilized (which it can be, with proper control).

Faceting of crystal surfaces is another valuable technique for obtaining single-atom sharp tips. Many crystal surfaces can exhibit faceting – the general methodology is to anneal the surface in the presence of an adsorbed thin layer of another material or in an applied electric field. The ad-layer or applied field is chosen to alter the relative surface energies of the tip's atomic planes in a specific way.

Then, annealing the tip under such conditions allows the low energy planes to expand and intersect, forming an atomically-sharp nano-pyramid at the tip apex.

Much of the initial surface science investigation of faceting systems such as the W(111) surface under adsorbed Pd (as well as other noble metals), W(111) under oxygen, and Ir(210) under oxygen was conducted by Ted Madey's group under LEED and STM investigation of the surfaces of bulk crystals [58–60]. Tien T. Tsong, who worked on FIM from its inception, has succeeded in transferring many of Madey's surface science systems to the apices of sharp FIM tips in order to engineer faceted single-atom tips [61–68]. All of these studies (with exception of the Ir(210) tips) involve the expansion of the (211) planes on a W(111) tip until its apex becomes a three-sided pyramid formed by the intersecting (211) planes (for reference, a W(111) tip can be seen in Fig. 5.4d). The faceting of the Ir(210) surface under oxygen exposure forms a pyramid from the (311), $(31\overline{1})$, and (110) planes with a single-atom apex pointed in the (210) direction [64].

Tip faceting by thermofield annealing (annealing under a large electric field) favors the growth of large (110) terraces. Applied to a W(111) tip, it can be used to create a pyramid in the opposite manner as described for noble metal plating – the (110) terraces expand until they intersect to form a three-sided pyramid at the expense of the (211) planes [69–72]. Thermofield annealing has the advantage of being carried out without the need for an adlayer of oxygen or metal on the tip surface.

The pyramidal geometry of faceted tips would be of considerable interest not only for atomically defined SPM experiments but also in atomic-scale nanoindentation experiments due to the simple relationship between their projected contact area and penetration depth (a desirable feature which is exploited in traditional nanoindentation testing [73]).

3.2.6 Tip Integrity: "Force Field" Protocol and Rest Gases

In order to carry out an SPM experiment with an atomically defined FIM tip, it is necessary to address issues of tip integrity. This is to ensure that when used in SPM, the apex is identical to that characterized in FIM. We will first discuss what is known about the reaction of gas molecules with the surface atoms of tungsten tips and then present a protocol to ensure that the tip structure remains intact between FIM and SPM. Another matter to be considered is how long the atomic structure of the tip is expected to last due to the finite rest gas pressure in UHV – this will determine how promptly an experiment must be performed such that the atomic configuration of the apex is known with reasonable statistical confidence.

The interaction of gases with metal surfaces was studied extensively in FIM by Erwin Müller (the inventor of FIM) at Penn State University, Gert Ehrlich at the University of Illinois at Urbana-Champaign, and Holscher and Sachtler at Shell Research in the Netherlands in the early 1960s. Here, we review the experimental findings for the adsorption of typical rest gases found in a UHV system (N_2, CO, O_2, H_2O, and H_2) on tungsten tips.

Nitrogen adsorbs on tungsten by dissociation, that is, as a single N atom chemically bound to a W tip atom [57]. When imaged, it appears brighter and larger than regular tip atoms [74]. However, the N-W bond is very strong and weakens the W's

bond to its neighbors. Due to the weakened substrate bonding, the N-W complex may field evaporate (as a unit [16]) at fields lower than those necessary for imaging [56]. Missing W atoms in an FIM image could therefore be an indication of N adsorption.

Carbon monoxide is less corrosive than N_2 [57]; however, it was still found to remove substrate atoms when field desorbed, leaving behind vacancies [75]. Oxygen corrodes tungsten in a manner similar to nitrogen, though less aggressively [57]. Again, the presence of oxygen is inferred by missing atoms [76]. Water was shown to remove tungsten atoms down to liquid He temperatures [57].

The adsorption of hydrogen has no corrosive effect on tungsten tips, nor can it be detected in FIM imaging [57, 77]. However, changes in field emission are detectable upon hydrogen adsorption.

In summary, the bonding of gas molecules to tungsten tips often occurs by dissociation of the molecule and a weakening of the bonding of the underlying W atom to its neighbors. The weakened backbonding leads to the phenomenon of adsorbate-induced field desorption during imaging. Therefore, both bright spots and missing W atoms in an FIM image are evidence of gas adsorption. For the interested reader, Table 5.1 recounts in more detail the results of adsorption studies of several types of gases on both tungsten and iridium tips.

Dedicated FIM systems have very stringent vacuum requirements due to their intended application to adatom diffusion. They are designed for high-temperature bakeout (limited to 300 °C by the microchannel plate (MCP)), and extreme procedures are carried out in order to minimize gas evolution [79].[4] In less ideal systems where the FIM is combined with other instrumentation (i.e., an SPM), one will likely have a larger concentration of corrosive gas molecules in the system during FIM imaging than under normal UHV conditions [80].[5]

Figure 5.10 demonstrates the rapid modification of an FIM tip by imaging gas impurities. Starting with the clean tip apex prepared by field evaporation (Fig. 5.10a), we momentarily lower the imaging voltage from 5.1 kV to 0 V and back (this procedure took 40 s). The image in Fig. 5.10b shows the changes that have occurred to the tip's atomic structure in this short time. This image is a color superposition image[6] in which the initial image appears in green and the subsequent image appears in red. Atoms which have been removed from the initial image are colored green, and those that have appeared in the second image are colored red. Both red and green sites are evidence of gas adsorption, and the $\sim$30 changes visible on the tip's 120 nm^2 surface area are certainly not encouraging to

[4]For example, the MCP is bombarded by 200 eV electrons for many days to remove gas atoms trapped in the channels.

[5]Even in the case of admitting ultrapure He through a heated quartz tube, the normal pumping speed of the UHV system may have to be sacrificed during FIM. In our case, the turbo pump must be valved off as the heated quartz cannot provide a sufficient flux of He to reach 10^{-5} mbar.

[6]A technique used by Müller with film and color photographic printing to identify individual changes among the many atomic sites on a FIM tip [81]. Here, it is done digitally.

the prospect of maintaining the atomic-scale tip structure long enough to do an SPM experiment with it!

Thankfully, all is not lost: due to the much higher ionization energy of He compared to all other gases [82], when large fields are applied to the tip (in the vicinity of the FIM imaging voltage), impinging gas molecules are easily ionized and will be repelled from the tip before they can chemically react with the tungsten atoms on its apex. We have found experimentally that reducing the tip voltage to ~80 % of the FIM imaging voltage is sufficient to prevent contaminant gases from reacting with tip atoms over extended periods of time. We call this the "force field" method and demonstrate its efficacy in Fig. 5.10b and c where no changes to the atomic structure of the tip can be identified.

Table 5.1 Adsorption and corrosion behavior of various gases on tungsten and iridium FIM tips

Gas	Tungsten tips	Iridium tips
$\mathbf{N_2}$	Adatoms appear bright, larger. Adatoms observed on highly corrugated planes and at steps – not within the close packed (110), but at the edges. More adatoms near (310) rather than (111) – this anisotropy is attributed to difference in N_2 dissociation rate [74]	N2 adsorbs as a molecule (without dissociation) between Ir atoms. Much less corrosive to Ir than it is to W (weaker bond) [57]
	Nitrogen binds strongly to W. Perturbed by the act of adsorption, the W can be field evaporated at regular imaging fields [56]	
	N binds on top of W sites (the N_2 molecule is dissociated, measured by mass spectrometry). Most N field desorbs before the ion emission is bright enough to be photographed (missing atoms could be sites of previously adsorbed N). W atoms were removed at fields lower than useful for imaging [57]	
	W-N complexes field desorb as a unit, reported in the first paper on the time-of-flight atom probe [16]	
CO	Found to be less corrosive than N_2. During FIM, CO is most corrosive when dissociated due to O adsorption on W which removes W substrate atoms. CO is dissociated by the energetic electrons removed from the He+ during the FIM process. Adding H_2, as a source of even higher energy electrons (in addition to the He imaging gas) enhanced the dissociation rate of CO [57]	Much less corroded than W [57]
	CO adsorption was found to rearrange substrate atoms. At 300 K, this leads to surface corrosion leading to vacancies underneath adsorbed molecules. Chemisorbed CO leads to "promoted field desorption" whereby the adsorbed species evaporates before it can be imaged, leaving behind a vacancy [75]	

(*continued*)

Table 5.1 (continued)

Gas	Tungsten tips	Iridium tips
O_2	Seems to be less corrosive than N2, but not as extensively studied [57]	
	W-O complexes are field desorbed together, observed in Ar ion FIM [78]	
	W-O complexes field desorb as a unit, reported in the first paper on the time-of-flight atom probe [16]	
	In He ion FIM, adsorbed oxygen cannot be directly observed on the surface; its presence is inferred from corrosion damage [76]	
H_2O	Studied in J. F. Mulson PhD thesis. Shown to remove W surface atoms (as well as Pt), even when surface is kept at liquid He temperature [57]	
H_2	Adsorption causes significant changes to the field emission pattern of the tip. However, no change can be detected in FIM. During FIM, a perturbation of the adsorbed H_2 layer is attributed to the bombardment of electrons coming from ionized He+ imaging gas [77]	H_2 could not be imaged, but removal of atoms, particularly in the bright (110) zone boundary, is attributed to H_2 adsorption [57]
	H_2 did not have a corrosive effect and could also not be detected [57]	

The following “force field” protocol is therefore suggested to preserve the tip apex from gas impurities in FIM/SPM experiments:

1. Prepare a clean tip by field evaporation in FIM.
2. Reduce applied voltage to ~80 % (“force field”).
3. Pump imaging gas, refill liquid nitrogen cold traps, flash TSP while “force field” is on.
4. Ramp down “force field” voltage when base pressure has recovered.
5. SPM experiment.

Finally, we must consider the fact that during the interval of the SPM experiment, the FIM tip will be subjected to contaminants in the UHV rest gas. We will consider the likelihood of rest gas molecules impinging on a 1.16 nm^2 area which corresponds to the area of the W(111) tip trimmer apex, plus the perimeter of the second layer of atoms on which it is supported [80]. The following estimations establish an upper bound on tip contamination as adsorption probabilities are considered to be unity.

The gas composition of the UHV rest gas was measured by a residual gas analyzer (RGA) (located in a different – but similarly pumped – UHV chamber used for sample preparation) yielding pressure fractions of the individual rest gas species, n_i. Using the total pressure reading of our measurement

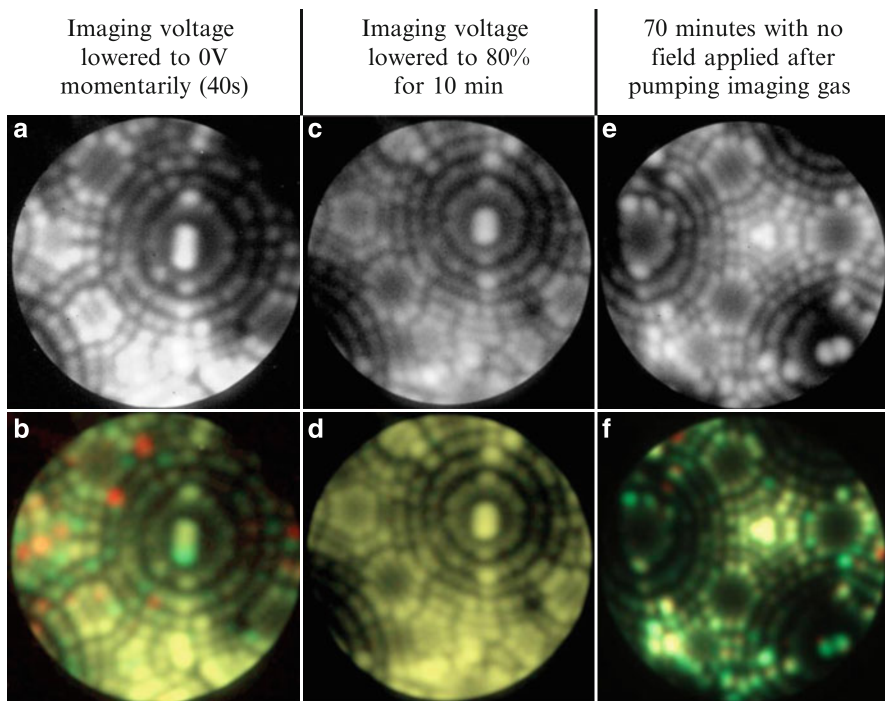

Fig. 5.10 (**a**) (110) tip at 5.1 kV; (**b**) color superposition image of (**a**) with the FIM image after the imaging voltage was momentarily lowered and raised – about 30 atomic sites show modifications; (**c**) (110) tip at 5.0 kV; (**d**) color superposition image of (**c**) with the FIM image after waiting 10 min with the voltage lowered to 4.0 kV – no changes are observed to the atomic structure; (**e**) (111) tip at 6.0 kV; (**f**) color superposition image of (**e**) with the FIM image after waiting 70 min in UHV (From Ref. [80] © IOP Publishing. Reproduced with permission. All rights reserved)

chamber gauge, $P_{\text{gauge}} = 5 \times 10^{-11}$ mbar, the partial pressures, p_i, of the component gases can be calculated from

$$p_i = n_i \frac{P_{\text{gauge}}}{\sum_i \frac{K_i}{K_{N_2}} n_i}, \tag{5.6}$$

where K_i/K_{N_2} is the ionization sensitivity of individual gas species relative to that of N_2 [83]. Combining the Maxwell-Boltzmann velocity distribution of the gas particles with the ideal gas law [84], we obtain the flux of each species as

$$F_i = \frac{p_i}{\sqrt{2\pi m_i k_B T}}, \tag{5.7}$$

where m_i is the atomic mass of the gas species, k_B is the Boltzmann constant, and T is the temperature.

The probability of k gas molecules arriving in area A on the tip during time τ is given by a Poisson distribution (assumes arrival is independent of time and location) [85]:

$$P(k) = \frac{e^{-FA\tau}(FA\tau)^k}{k!}. \quad (5.8)$$

The probability of obtaining more than one arrival on the tip apex area (i.e., $k > 1$) can be easily obtained using the property that the distribution is normalized:

$$P(k > 1) = \sum_{k=1}^{\infty} P_k = 1 - P_0 = 1 - e^{-FA\tau}. \quad (5.9)$$

The rate of tip contamination is described in two ways: In the first way, we calculate the duration of an experiment such that in 5 % of experiments of this duration, more than one gas molecule would have impinged on the apex (i.e., on average, 1 in 20 experiments having this duration would be carried out with a modified tip). In the second way, we calculate the probability of more than one gas molecule impinging on the apex during a 60 min delay (chosen as a minimum reasonable SPM experiment duration which must include tip transfer, sample approach, etc.). The results of these calculations are shown in Table 5.2. Note that other unidentified gases (not listed) make up 2.2 % of the gas composition, meaning they have approximately the same statistics as N_2.

We notice immediately that hydrogen is problematic because of its high pressure fraction and flux (the latter due to its low mass). However, its presence goes undetected in the methods employed here – FIM characterization is blind to hydrogen, and it is known to have no corrosive behavior to tungsten tips [57]. After hydrogen, the next most common gases (H_2O, N_2, and CO) are at a nearly acceptable background level if an experiment is completed within a short period of time ($\sim$1 h).

Figure 5.10e illustrates the typical rest gas contamination of our tungsten tips which have been preserved with a "force field" until the UHV system had returned to base pressure. The tip was left in UHV for 70 min after the "force field" was turned off. The color superposition image in Fig. 5.10f shows changes to $\sim$30 atomic sites. (The number of changes is overestimated due to contamination during the FIM start-up procedure [80].) Assuming an approximate mass of 28 amu, the changes to the tip during this time interval indicate an effective contaminant pressure of $\sim 2 \times 10^{-11}$ mbar. This number is consistent with the calculations presented in Table 5.2 and the expected overestimation of contamination due to the FIM start-up procedure.

Experiments with atomically defined tips must be performed quickly, even in a clean UHV environment. This has important consequences for the design of a combined FIM/SPM experiment: since the sample should also not be subjected to contamination from the imaging gas, the tip (or sample) must be transferred from a separate vacuum chamber in a reasonable time frame, and the coarse approach of the tip to the sample surface must be done with minimal delay.

Table 5.2 Table of typical UHV rest gas species, their partial pressures, fluxes, and calculated contamination times and probabilities for a 1.16 nm^2 tip apex. H_2O is likely overestimated due to the RGA location in the sample preparation chamber which is not as thoroughly baked and is subjected to the regular introduction of new samples (From Ref. [86]. © IOP Publishing. Reproduced with permission. All rights reserved)

Species	Mass, m (amu)	Ionization sensitivity, K_i/K_{N_2}	Pressure fraction, n_i	Partial pressure, p_i (mbar)	Flux, F (nm^{-2} s^{-1})	1:20 apex contamination time (min)	P(k > 1) gas atom on apex during a 60 min delay
H_2	2	0.42	88.0 %	9.4E-11	1.0E-03	0.7	98.5 %
H_20	18	0.9	4.6 %	4.9E-12	1.8E-05	41	7.1 %
N_2	28	1	2.3 %	2.4E-12	7.0E-06	100	2.9 %
CO	28	1.2	1.7 %	1.8E-12	5.2E-06	140	2.1 %
CO_2	44	1.4	1.1 %	1.2E-12	2.7E-06	270	1.1 %
He	4	0.16	0.1 %	1.1E-13	8.1E-07	890	0.3 %

3.3 Key Research Findings

3.3.1 Review of Combined FIM/SPM Experiments

A handful of groups pioneered the combination of FIM and SPM from the mid-1980s to the late 1990s. Here, we review the work of the principal groups in this field in an approximately chronological order.

The first report of combined FIM and STM techniques was from Kuk and Silverman working at AT&T Bell Laboratories in New Jersey. Their investigation focused on the observed corrugation height (constant current STM topography) of the rows of the (1 $\times$ 5) reconstructed Au(100) surface using a W(100) tip at room temperature [87]. The same results also appear in a well-cited paper about STM instrumentation published in 1989 [88]. We are not aware of any further publications containing FIM results from these authors.

Toshio Sakurai's group from Tohoku University in Sendai, Japan, published quite extensively about combined FIM and STM in a technique they refer to as field ion-scanning tunneling microscopy (FI-STM). By 1989, Sakurai had built a series of room-temperature FI-STMs [89]. A review article on the FI-STM technique appeared in Progress in Surface Science in 1990 [90]. In the early 1990s, the group focused on silicon surfaces and worked to study the surface bonding of C_{60} molecules [91–93] and alkali metals [94]. In these studies, the FIM was used to confirm tip cleanliness and sharpness in order to help obtain reliable atomic resolution in STM. The role of the tip's atomic structure in STM imaging was not an explicit concern in this work. The group of Yukio Hasegawa, who worked with Sakurai, later demonstrated FIM characterization of a tip mounted to a length extension resonator for AFM [95].

Some very diligent combined FIM/STM work was carried out by Masahiko Tomitori et al. while based at the Tokyo Institute of Technology, Yokohama, Japan, between ~1990 and 1996. The first work investigating STM tip approach was performed in air on freshly cleaved highly oriented pyrolytic graphite (HOPG), and the Pt-Ir alloy tips were transferred to and from vacuum for FIM characterization [96]. The goal was *not* to implement atomically defined tips in air; they wanted to ensure that the tip apex did not crash into the substrate inadvertently during coarse approach. Tomitori underlined the necessity in performing the tip approach within the bandwidths of the STM feedback loop and current preamplifier – exceeding these bandwidths could result in crashing the tip without any sign of a current spike arising from mechanical contact. Approaching the tips too quickly was found to render the tip apex nonobservable in FIM; a large amount of carbon, hydrogen, and oxygen had also been transferred to the tip apex, detected by a time-of-flight (ToF) mass spectrometer.

In 1996, Tomitori published scanning tunneling spectroscopy (STS) results with a "buildup" pyramidal tip in UHV [97]. The motivation here was to try to develop an experimental procedure to obtain reproducible STS data by controlling the tip geometry – that way, the STS technique could be more straightforwardly applied to unknown samples. STS was carried out on the Si(111)-7 $\times$ 7 surface in 64 $\times$ 64 point arrays in order to average over the surface unit cell, and spectra were found to be reasonably repeatable with the tips as long as the bias range was kept within

−2 to +2 V. Tips retained similar patterns in field emission microscopy (FEM)[7] with slightly modified voltage thresholds for imaging (perhaps indicating slight tip changes). Expanding the STS bias range to −3 to +3 V altered the STS spectra radically, and FEM showed large changes present on the tip, attributed to the transferral of Si atoms from the substrate.

These two studies by Tomitori provided valuable early insights into the implementation of atomically defined tips in STM: feedback and current detection bandwidths must be respected to avoid tip crashing on approach, FEM might be a less awkward way than FIM to check for tip changes due to the absence of potentially corrosive imaging gas, and STS can be implemented without significant tip changes as long as the bias voltages are kept within a small enough range (±2 V).

At the University of Arizona, a combined STM with a ToF atom probe was built by Uwe Weierstall and John Spence in the mid-1990s. They called the instrument the scanning tunneling atom probe (STAP), and it was intended to be a means of supplementing the STM with chemical identification in a kind of "atomic tweezer." The goal of this instrument was to transfer a chemically unknown species from the sample to the tip, say by pulsing the STM bias voltage, and then switch over to ToF mode to identify the chemical species ejected from the tip. Their first report in 1996 demonstrated the proof of concept of the STAP [98]. The atom probe's mass-to-charge detection was calibrated by W^{3+} and W^{4+} field evaporated from tungsten tips, and the authors presented a preliminary result measuring a handful of Si atoms transferred from an Si(111)-7 × 7 surface to a tip apex, as identified both in STM imaging and ToF mass spectrometry.

A second and final paper from this instrument was published in Surface Science in 1998 [99]. Although FIM-characterized tip apices were not an objective of their work, some aspects of this second paper are relevant to the implementation of atomically defined tips in current endeavors. ToF revealed that some care had to be taken in order to not overshoot the tunneling current set point upon initial approach and transfer Si atoms from mechanical contact (also noted by Tomitori). The authors report statistics on an impressive number of experiments: after improving their tip approach procedure, in ~80 % of about 50 experiments, W tips could be scanned and returned for ToF analysis without having picked up Si atoms. In ~20 % of cases, a tip change occurred while scanning, often accompanied by a sudden improvement in STM resolution, and this correlated with the ToF detection of Si transferred to the probe tip.

Although single-ion sensitivity is possible with their chevron microchannel plate, the open area of the detection channels is only ~60 %. Nevertheless, the statistics are quite convincing that W tips can be approached to tunneling proximity in STM without the transferral of atoms from the substrate, but tip changes seen during STM scanning correlate with atom transfer. FIM imaging of the tip was not a

[7]FEM operates in a similar manner to FIM, but a field emission current is detected rather than field ionized gas atoms. A spatial map of the field emission current is visualized on an MCP/phosphor screen when the tip is negatively biased. The technique does not allow the atomic structure of the tip to be imaged.

goal of this work, but the studies are valuable from the standpoint of considerations of material transfer which would modify atomically defined FIM tip apices when they are used in STM.

Manfred Leisch's group at the Graz Institute of Technology, Graz, Austria, built a position-sensitive atom probe detector to be used in conjunction with a commercial Omicron STM-1. The goal of this system was to investigate the mechanical interaction between materials on the atomic scale [100]. This was essentially an experimental realization of the systems studied in early molecular dynamics simulations to address atomic-scale contact formation, wetting, adhesive bonding, connective neck formation, and plastic deformation [101]. The experimental investigation of mechanical interactions between tips defined in FIM and other specimens was not particularly new – this had been investigated to some extent in the 1960s and 1970s by Müller and Nishikawa [102], but the lack of control over interaction forces between the tip and contacting specimen made it difficult to avoid destroying the delicate FIM tip. Leisch's group identified that the techniques developed for SPM (e.g., piezoelectric transducers, force, and current feedback methods) were ideal for controlling mechanical interactions with FIM tips at atomic length scales. Using STM control of the tip and a time-of-flight mass spectrometer incorporated into the FIM, the number of atoms transferred from the substrate to the tip during indentation could be counted. The authors also made interesting observations about changes to the tip structure induced by STM imaging [103].

3.3.2 Atomically Defined Tips in STM

In Sect. 3.2.6, we introduced the "force field" protocol to ensure that tip apices remain unchanged between FIM and SPM, and we have also determined that they can be kept atomically clean for a reasonable length of time for use in the SPM experiment. Now, we report experimental results on bringing tips into tunneling proximity with SPM samples.

Tomitori identified the necessity to keep the tip approach speed within the detection bandwidth to avoid set point overshoot (which would result in tip crashing; Sect. 3.3.1) [96]. In the case of STM where the tunneling current increases at a rate of about one decade per angstrom, dangerous overshoot can be avoided by limiting the approach speed to a maximum of $\sim$1,000 Å/s. This is to allow sufficient time for the distance regulation feedback loop to respond to regulate the tip distance (a standard tunneling current amplifier has a bandwidth of a couple kHz, and typical SPM feedback loops are tuned to respond in about $\sim$1 ms). We approach tips at a speed of 200 Å/s, resulting in negligible overshoot.

It turns out that the choice of substrate is very important in maintaining tip integrity. We have investigated tip integrity after approaching FIM tips to several types of STM samples: after reaching the tunneling set point and maintaining this distance for a few minutes, tips were retracted and imaged again in FIM [80]. With confidence that relatively few tip changes occur under this time delay due to the rest gas (Sect. 3.2.6), we can study the effect of the interaction with the sample on the tip structure.

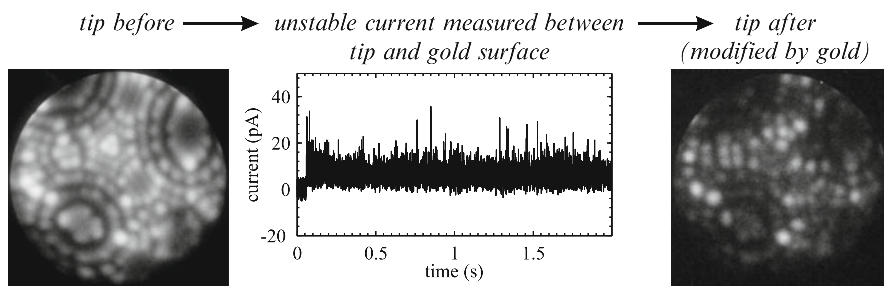

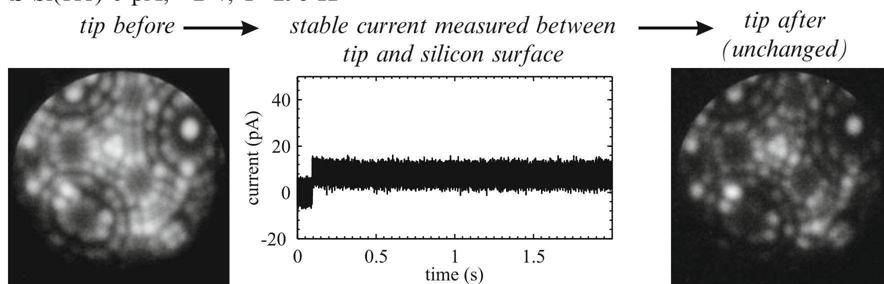

Fig. 5.11 FIM images before and after tunneling experiments with (**a**) Au(111) and (**b**) cleaved Si(111) at room temperature. Tunneling current snapshot shows the initial moment of approach of the tip to the sample surface

We summarize the approach of W(111) FIM tips to Au(111) and cleaved Si(111) surfaces in Fig. 5.11. In both cases, the tip is approached to a tunnel current set point of 6 pA. In the case of the Au(111) surface (Fig. 5.11a), the measured current is very unstable – many spikes are apparent up to ~40 pA throughout the experiment. The tip is imaged again in FIM and reveals changes to the atomic structure in approximately the entire field of view. Note that the underlying threefold symmetry is still visible which indicates that the tip did not suffer mechanical damage during the experiment (the large flat W(110) planes are mostly intact).

The observation of spikes and correlated FIM tip changes for Au(111) is consistent with many other experiments on Au(111), as well as cleaved HOPG, sputter-annealed InSb(001), and cleaved GaAs(001) [29].[8] The presence of changes to the tip apex must be due to interaction with the sample – the "force field" protocol is very successful – but do the atoms which change the tip structure come from the sample itself? Or could they be gas atoms physisorbed on the tip

[8]Though the frequency of spikes was very much less on some of these substrates, their presence was still correlated with changes to the FIM tip.

shank that migrate to the apex under the electric field gradient in STM? In order to understand where the changes come from, we turned to cleaved Si(111), the most reactive surface that could be easily prepared on our system [86].

Figure 5.11b shows that the tunneling current is exquisitely stable between FIM tip and Si(111) surface. It also confirms that very little overshoot occurs when the sample surface is first detected at 0.1 s. The tip apex is unchanged in the image taken after the experiment. The strong correlation between spikes in the tunneling current and tip changes visible in FIM suggests that material is transferred from the sample surface to the tip. The changes to the tip are not due to gas molecules from the shank – if this were the case, the experiments with a Si(111) surface would be equally affected.

The temperature dependence of the tunnel current spikes and tip changes has also been investigated for Au(111) by cooling the entire microscope (sample and tip) to 158 K [104]. As Fig. 5.12 indicates, the magnitude of the current spikes is much higher at low temperature (the vertical scale is the same in both Fig. 5.12a, b). Interestingly, at low temperature, the modifications to the tip apex are confined to the very center of the tip. The thermally activated diffusion of adatoms on the tip is expected to be quenched at this temperature due to the large corrugation of the W(111) surface [104]; therefore, the transferred atoms stay in place.

Though the result of localized tip modifications precludes Au(111) at 158 K as a possible substrate for atomically defined tips in STM, it is a useful result for two reasons: Firstly, it provides additional evidence that the changes to the tip, which are localized to the very apex, originate from atoms transferred from the sample rather than the tip shank.[9] Secondly, it indicates that the expected W(111) crystal plane is indeed the part of the tip which interacts with the sample (i.e., the (111) direction is pointed along the tip wire axis, even after tip fabrication/etching/preparation procedures).

In order to carry out an experiment with an atomically defined tip, it is also important to be able to identify events indicative of tip changes. In experiments on cleaved Si(111), where the tunneling current is mostly stable, occasional tip changes can take place while scanning. These tip changes are characterized by simultaneous spikes in the tunneling current of order 50–100 pA (at 8 pA set point), accompanied by changes in topographic scan height on the order of 10 pm (up to 130 pm), and often changes in the lateral resolution of the STM image [29]. We expect that the $\sim$10 pm changes, which are very much smaller than interatomic distances in crystals, may arise from a transferred atom which diffuses to a site slightly off-center and weakly modifies the electronic density of states of the apex atoms which are involved in tunneling.

Point defects on the cleaved Si(111) surface also provide an opportunity to study tip changes because they image the tip itself in the form of an image convolution. The tip structure is reflected in features repeated throughout the image.

[9]If the latter were the case, tip changes would be seen all over the apex region from chemically bound atoms.

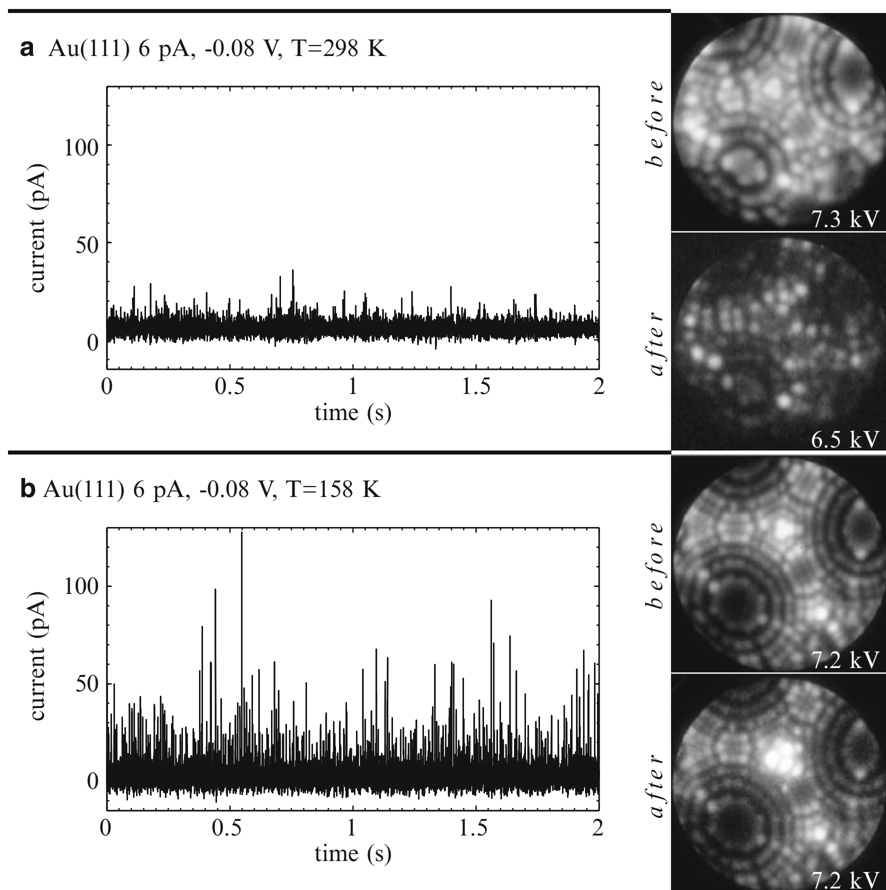

Fig. 5.12 FIM tip apices before and after, as well as a snapshot of the measured tunneling current when approached to Au(111) at temperatures of (**a**) 298 K and (**b**) 158 K

For example, in Fig. 5.13a, b, a 2-lobed feature recurs in the constant current STM image. We can draw a ball-and-stick model of this feature to scale (and in the correct orientation) with the initial FIM image of the tip (Fig. 5.13e). This gives some appreciation of where the STM imaging atoms (added by tip changes) might be located with respect to the original tip geometry. The tip convolution features change as STM scanning is continued, and another repeated motif is shown in Fig. 5.13c, d for negative and positive biases, respectively.

As expected from the changing tip convolutions, the STM tip appears highly modified when it is returned to FIM for imaging (Fig. 5.13f). It is imperative to realize that the image displayed in (f) is just *one* image of many that are taken of the tip structure which evolves during imaging due to field evaporation. FIM carried out on a highly modified tip is a very unstable process for several reasons: the added atoms protrude from the surface, so the electric field is locally enhanced at their

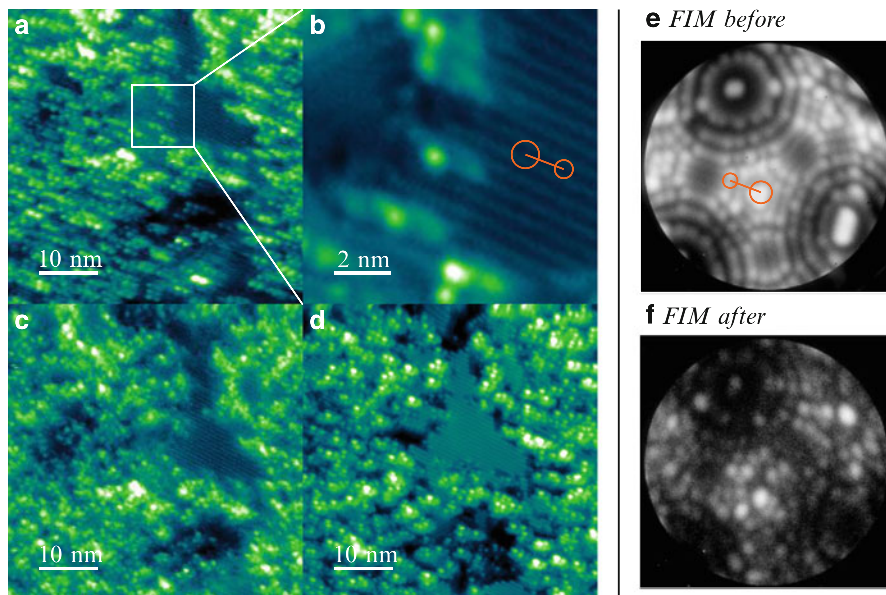

Fig. 5.13 (**a**) STM image showing a partially reconstructed Si(111) terrace. (15 pA, +2 V) (**b**) higher magnification image of a region shown in (**a**) highlighting the tip convolution feature. (15 pA, +2 V) (**c**) Filled-state STM image of the same area after tip changes. (15 pA, −2 V) (**d**) Empty state STM image of the same area. (15 pA, +2 V) Lines running in the 10-o'clock to 4-o'clock direction correspond to the 2×1 surface reconstruction. (**e**) FIM image before STM experiments with tip convolution model scaled to the appropriate size and direction. (6.4 kV) (**f**) FIM image after extensive STM experiments. (6.2 kV)

positions, leading to their facilitated field desorption.[10] Because of their different chemical nature, they will be subject to ionization and desorb at lower voltages than tungsten would (the ionization field of almost every other atomic species is lower than that of tungsten [12]). Because of the unstable atomic structure during FIM imaging of a modified tip, it would be inappropriate to compare the image in Fig. 5.13f to the features of the topographic STM images.

A concluding word of caution when inspecting FIM tips after STM experiments: the tip is made from a crystal and is therefore self-similar. After field evaporating three atomic layers from the apex, it will appear nearly indistinguishable from the original tip.[11] It is possible for the experimenter to be misled into thinking that the

[10]The images of modified tips that we display are taken at as low a voltage as possible to minimize tip changes, but it is impossible to determine how many atoms desorb before the onset of imaging. Numerous images are acquired while the voltage is slowly increased; they are averaged together in sets where the tip structure remains constant. The stability of modified tips may increase with decreasing temperature. However, changing the temperature will not change the ionization field of the adsorbed atoms relative to tungsten or the imaging gas.

[11]It takes many layers of field evaporation to increase the radius significantly.

post-STM tip is unchanged when he or she is in fact observing a new layer of atoms. With the present availability of digital cameras and plentiful data storage, it should be possible to acquire many frames and carefully assess the results.[12] We urge caution in the interpretation of early combined FIM/SPM studies which do not discuss the fragility of tungsten tip apices due to their reactivity, the stability of the tunneling current in STM, or the FIM imaging process after STM [87, 105].

At the time of writing, we are confident that STM imaging with pristine FIM tips can be carried out, albeit for a very short period of time (~1 min to first tip change on cleaved Si(111)). Tip changes are identified during STM scanning by discontinuities in tip height, spikes in the tunneling current, and changes to STM resolution. At room temperature, highly reactive sample surfaces are needed to reduce the population of mobile adatoms on the surface which can transfer to and alter the tip. Operating the experiment at a sufficiently low temperature to freeze out adatom motion on the sample is another promising route to achieve atomically defined FIM tips in SPM.

3.3.3 Long-Range Force Interactions in Noncontact AFM

The advent of new force sensors for noncontact AFM, namely, the qPlus [30] and the length extension resonator [31, 32], has allowed tungsten FIM tips to be used in noncontact AFM where until recently, microfabricated silicon cantilevers had been most popular. FIM imaging of tip apices on length extension transducers has been demonstrated by An et al. [95, 106], noting that field evaporation is a very effective tip preparation technique for removing the surface oxides from tungsten. The successful FIM characterization of a tip on a qPlus transducer was recently reported by Falter et al. in 2013 [51]. This work constitutes a substantial advance in the use of well-characterized tips because the authors use the FIM data in a quantitative way to understand noncontact AFM results.

Falter et al. use the overall tip radius (from FIM) and cone angle (from supplemental SEM measurements) as input to models for electrostatic [107] and van der Waals forces [108] acting between a spherically capped conical tip and a flat surface. The authors were able to identify a strong variation of the contact potential with distance at tip-sample separations less than 2 nm, indicating that the inhomogeneous work function of the faceted tip surface contributes localized patch charges to the electrostatic force response. Detailed electrostatic models of SPM tips based on FIM characterization may also help to elucidate atomic-scale contrast in the contact potential measured by Kelvin probe force microscopy (KPFM) [109, 110].

3.3.4 FIM Tips for Atomic-Scale Nanoindentation

In order to understand the mechanics of deformation during indentation, atomistic simulations are often employed to provide a view "inside" materials while an

[12] In order to screen for tip changes during the STM experiment itself, one may want to acquire a higher bandwidth version of the tunneling current signal throughout the entire experiment to scrutinize carefully for spikes. By higher bandwidth, we mean the several kHz bandwidth of the current preamplifier, rather than the ~100 Hz pixel STM scan rate.

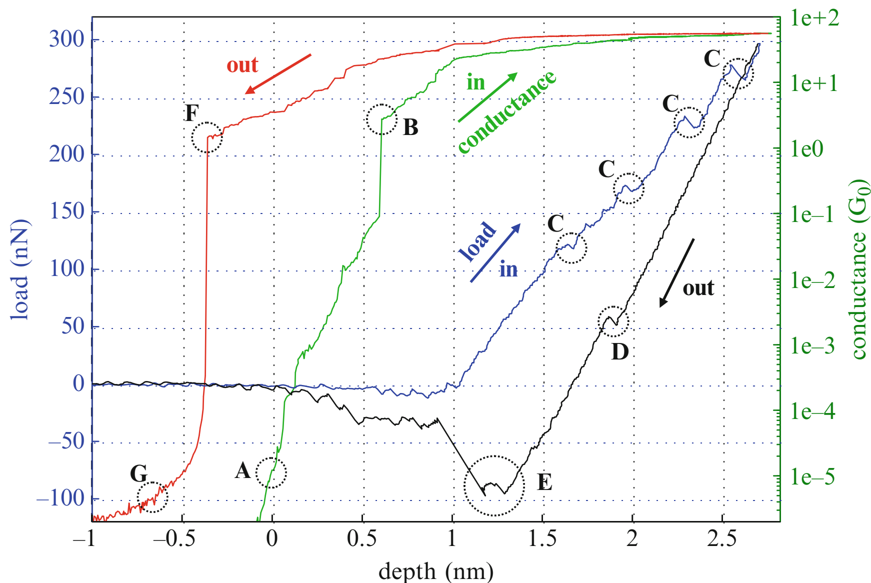

Fig. 5.14 A load-displacement curve showing important features in atomic-scale nanoindentation response (see text). Load is *blue* and conductance is *green* upon loading the contact (in-direction), load is *black* and conductance is red upon unloading the contact (out-direction)

indentation stress is applied [111]. These computer simulations are typically limited to some millions of atoms and thus probe a much smaller volume than in traditional nanoindentation. To close the length scale gap, the lateral size of indentation experiments must be diminished by about three orders of magnitude. Nanometer-sized indenters are also fundamentally interesting due to the breakdown of continuum mechanics at this length scale – spherically shaped crystals contain stepped facets which are expected to modify the contact pressure distribution when used for indentation [112].

Preparation of tips by FIM is an ideal way to obtain a clean, atomically characterized spherical apex with a radius of several nanometers. The strong covalent bonding of tungsten gives the material stable performance under the high electric fields of He ion FIM and makes it exceptionally hard [113]. High hardness is essential to ensure that deformation occurs in the substrate rather than the indenter.

Using a combination of FIM, STM, and AFM (introduced in Fig. 5.1), we have investigated the indentation response of Au(111) under indentation by FIM-characterized tips [27, 29, 114–118]. We now discuss results of recent experiments.

Referring to Fig 5.14, we now present typical features of an atomic-scale nanoindentation curve in which a W(111) FIM tip is indented into a Au(111) single crystal. The zero point of the indentation depth is set to the crossing of the 1 GΩ resistance of the conductance data ($1 \times 1\,0^{-5}$ G_0 in the example shown). This is a

semi-arbitrary zero point because zero separation is not well defined at these length scales. A jump-to-contact is observed in the current (green) at point B where the junction conductance suddenly increases to $\sim 3G_0$. At the points labeled C, abrupt mechanical rearrangements occur in which the load decreases and depth increases simultaneously (the slope of these changes corresponds to the stiffness of the force transducer). These events are known as pop-ins and are attributed to the sudden nucleation of plastic damage in the sample [119]. A pop-out is registered at point D, interpreted as an event which partially reverses the plasticity created during loading. The large adhesion force of the metallic contact is shown at point E. The conductance upon unloading (red) shows a large hysteresis indicative of wire drawing. This atomic-sized wire finally breaks at a conductance of just over 1 G_0 at point F. G is an artifact from the long settling time of the current preamplifier and should not be interpreted physically.

The adhesion of clean nanoscale contacts is remarkable in magnitude and is a key factor differentiating response in these experiments from those of a traditional nanoindenter. The two reasons for this are the exceptional cleanliness of the indenter/surface system prepared in UHV and the large surface-to-volume ratio at small length scales where energies required to create new surfaces are comparable to those required to deform volumes [120]. Using FIM prepared tips, a strong dependence of adhesion on the state of the tip has been observed [117]. After preparing an atomically clean tungsten surface by field evaporation in FIM, the tip was repeatedly indented into the pristine surface of a Au(111) single crystal. As indentation progressed, the adhesive force dropped by a factor of 6× with a 1/e rate of 11–14 indentation cycles, indicating that the surface composition of the tip (in this case, wetted by the gold substrate) strongly affects the measured mechanical behavior. The FIM is therefore an ideal tool to create an experimental indentation system with a well-defined surface composition for quantitative comparison with atomistic simulations.

The determination of contact area and stresses during indentation depends on accurate indenter characterization. With FIM-characterized W(111) indenters, the minimum threshold for plasticity was investigated in Au(111) [116]. The indenter is pictured in Fig. 5.15a, and stochastically initiated plasticity on the Au(111) single crystal surface is shown in Fig. 5.15c before and d after indentation. The broad distribution of yield-point shear stress suggested that dislocations were heterogeneously nucleated in this system. The resolution of very low forces and displacements in AFM also permitted the extraction of energies required to produce defects in the gold substrate: surprisingly, permanent impressions are left in the substrate by a mechanical energy expenditure of only $\sim$70 eV.

The contact area during indentation, which can be inferred from the FIM tip geometry, also yields important insights about electronic transport through the indentation-formed nanocontact [115]. Experiments using a W(111) tip and Au(111) sample yield a highly variable conductance in the range of 0.02–4.9 G_0/nm^2, which is much less than a Sharvin estimation of $\sim 13.8\ G_0/nm^2$. (The latter is expected when each atom in the metallic contact contributes $\sim 1\ G_0$ to the conductance.) The reason for the much reduced conductance between the W(111) and

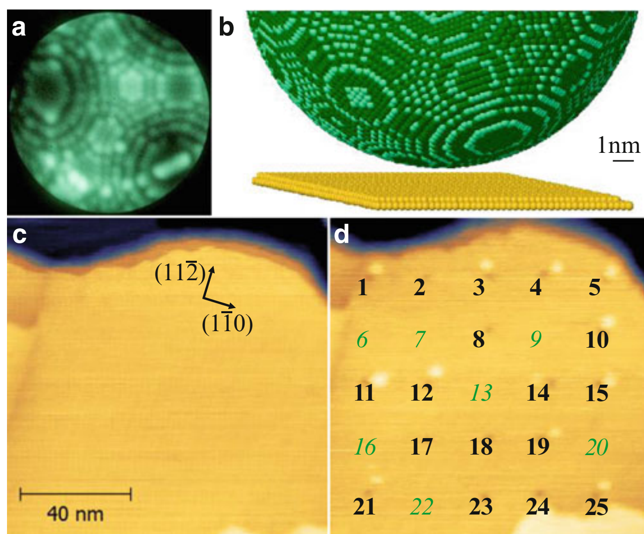

Fig. 5.15 (**a**) FIM image of the W(111) indenter (5.5 kV tip voltage); (**b**) ball model of a W(111) with a 9.5 nm radius and Au(111) substrate to scale; (**c**) Au(111) terrace before and (d) after a 5 × 5 indentation array with 20 nm spacing between indents (20 pA, −0.05 V sample bias). *Bolded numbers* indicate plastic sites, and *italicized numbers* indicate elastic sites (From Ref. [116]. Copyright 2013 by the American Physical Society)

Au(111) metals was clarified by first-principles density functional theory calculations: the d-wave electron modes of tungsten are poorly approximated by the *s*-wave modes of gold, resulting in backscattering of electrons at the interface. Furthermore, disorder and vacancies are also expected to diminish electron conduction. Electronic transport across interfaces has obtained considerable attention in theoretical work [121–124], but the experiments are rare due to the challenge in determining the contact area in nanoscale systems [125, 126]. Because the geometry of FIM tips can be easily modified by starting with wires of different crystal orientations and can be rotated with respect to SPM substrates, one might expect them to find use in the study of the electronic transparency of interfaces and disorder structures.

3.4 Conclusions and Future Perspective

Atomic-scale characterization of SPM tips by FIM provides a detailed view of the tip structure which is usually unknown in SPM experiments. We have discussed the operating principle and resolution of FIM, the preparation and radius determination of the probes, and advanced tip preparation by techniques such as gas etching and surface faceting.

In the implementation of FIM tips in SPM, we considered tip integrity with regard to modifications due to chemical reaction with impurities in the imaging gas and with UHV rest gases. We outlined the "force field" protocol which inhibits

changes to the tips, guaranteeing the transferral of a pristine apex to the SPM tip-sample junction.

At the moment, STM with a stable atomically defined tip has yet to be demonstrated: at room temperature, tip changes occur within a short period of time on many kinds of substrates. We expect that stable tips should be obtainable with the construction of a stable cryogenic SPM with in situ FIM or with the use of very reactive samples, such as Si(111)-7 $\times$ 7, at room temperature. Resolving the issues of tip changes is an essential challenge to overcome in order to move the field into more ambitious experiments such as the characterization of atomically defined molecular junctions, quantitative understanding of local electrostatic forces from faceted tips, and their use as benchmarking probes for materials with exotic electronic properties (e.g., oxide electronics).

Their well-defined radii and chemical composition makes FIM tips ideal for atomic-scale indentation. There are many open questions in this area which can be experimentally addressed in detail, such as indentation by stepped indenters of different geometries and surface chemistries. There is ample opportunity to borrow techniques of advanced tip preparation (such as faceting) from the FIM community and apply them to the study of nanomechanics, as well as the study of electronic transport through mechanically formed nanocontacts.

References

1. Fink H-W (1986) Mono-atomic tips for scanning tunneling microscopy. IBM J Res Dev 30(5):460–465
2. Giessibl FJ, Hembacher S, Mannhart J (2004) Force microscopy with light-atom probes. Science 305(5682):380–383
3. Campbellová A, Ondrácek M, Pou P, Pérez R, Klapetek P, Jelínek P (2011) 'Sub-atomic' resolution of non-contact atomic force microscope images induced by a heterogeneous tip structure: a density functional theory study. Nanotechnology 22(29):295710
4. Hofer WA, Redinger J (1998) Electronic structure of a realistic STM tip: the role of different apex atoms. Philos Mag Part B 78(5):519–525
5. Kwapinski T, Jalochowski M (2010) Signature of tip electronic states on tunneling spectra. Surf Sci 604(19–20):1752–1756
6. Sugimoto Y, Pou P, Abe M, Jelínek P, Pérez R, Morita S, Custance O (2007) Chemical identification of individual surface atoms by atomic force microscopy. Nature 446(7131):64–67
7. Ternes M, González C, Lutz CP, Hapala P, Giessibl FJ, Jelínek P, Heinrich AJ (2011) Interplay of conductance, force, and structural change in metallic point contacts. Phys Rev Lett 106(1):016802
8. Wagner RJ, Ma L, Tavazza F, Levine LE (2008) Dislocation nucleation during nanoindentation of aluminum. J Appl Phys 104(11):114311
9. Shin C, Osetsky Y, Stoller R (2012) Dislocation nucleation and defect formation in copper by stepped spherical indenter. Philos Mag 92(25–27):3158–3171
10. Mehrez H, Wlasenko A, Larade B, Taylor J, Grütter P, Guo H (2002) I-V characteristics and differential conductance fluctuations of Au nanowires. Phys Rev B 65(19):195419
11. Müller EW (1951) Das Feldionenmikroskop. Z Phys 131(1):136–142
12. Tsong TT (1990) Atom-probe field ion microscopy. Cambridge University Press, New York

13. Antczak G, Ehrlich G (2010) Surface diffusion. Cambridge University Press, New York
14. Gault B, Moody M, Cairney JM, Ringer SP (2012) Atom probe crystallography. Mater Today 15(9):378–386
15. Miller MK, Kelly TF, Rajan K, Ringer SP (2012) The future of atom probe tomography. Mater Today 15(4):158–165
16. Müller EW, Panitz JA, McLane SB (1968) The atom-probe field ion microscope. Rev Sci Instrum 39(1):83
17. Panitz JA (1973) The 10 cm atom probe. Rev Sci Instrum 44(8):1034
18. Lee HJ, Ho W (1999) Single-bond formation and characterization with a scanning tunneling microscope. Science 286(5445):1719–1722
19. Stipe BC, Rezaei MA, Ho W (1998) Single-molecule vibrational spectroscopy and microscopy. Science 280(5370):1732–1735
20. Zhou W, Wang ZL (eds) (2006) Scanning microscopy for nanotechnology. Springer, New York
21. Binnig G, Rohrer H (1987) Scanning tunneling microscopy – from birth to adolescence. Rev Mod Phys 59(3):615–625
22. Chen CJ (2008) Introduction to scanning tunneling microscopy, 2nd edn. Oxford University Press, Oxford
23. Stroscio JA, Kaiser WJ (eds) (1993) Scanning tunneling microscopy, 1st edn. Academic, San Diego
24. Sarid D (1994) Scanning force microscopy. Oxford University Press, New York
25. Giessibl FJ (2003) Advances in atomic force microscopy. Rev Mod Phys 75(3):949–983
26. Hauptmann N, Mohn F, Gross L, Meyer G, Frederiksen T, Berndt R (2012) Force and conductance during contact formation to a C 60 molecule. New J Phys 14(7):073032
27. El Ouali M (2010) Nanometre scale indentation: effect of very sharp indenters on adhesion, plasticity, and electronic transport. PhD thesis, McGill University
28. Hagedorn T (2010) Atomic contacts characterized by force and current. PhD thesis, McGill University
29. Paul W (2013) Atomically defined tips in scanning probe microscopy. PhD thesis, McGill
30. Giessibl FJ (1998) High-speed force sensor for force microscopy and profilometry utilizing a quartz tuning fork. Appl Phys Lett 73(26):3956
31. Bartzke K, Antrack T, Schmidt K-H, Dammann E, Schatterny CH (1993) Needle sensor-a micromechanical detector for atomic force microscopy. Int J Optoelectron 8:669
32. Michels A, Meinen F, Murdfield T, Göhde W, Fischer UC, Beckmann E, Fuchs H (1995) 1 MHz quartz length extension resonator as a probe for scanning near-field acoustic microscopy. Thin Solid Films 264(2):172–175
33. Dürig U, Novotny L, Michel B, Stalder A (1997) Logarithmic current-to-voltage converter for local probe microscopy. Rev Sci Instrum 68(10):3814
34. Schönenberger C, Alvarado SF (1989) A differential interferometer for force microscopy. Rev Sci Instrum 60:3131
35. Lalanne J-B, Paul W, Oliver D, Grütter PH (2011) Note: electrochemical etching of sharp iridium tips. Rev Sci Instrum 82(11):116105
36. Miller MK, Cerezo A, Hetherington MG, Smith GDW (1996) Atom probe field ion microscopy. Oxford University Press, Oxford
37. Lucier A-S, Mortensen H, Sun Y, Grütter PH (2005) Determination of the atomic structure of scanning probe microscopy tungsten tips by field ion microscopy. Phys Rev B 72(23):235420
38. Ibe JP, Bey PP, Brandow SL, Brizzolara RA, Burnham NA, DiLella DP, Colton RJ, Lee KP, Marrian CRK (1990) On the electrochemical etching of tips for scanning tunneling microscopy. J Vacuum Sci Technol A 8(4):3570
39. Melmed AJ (1991) The art and science and other aspects of making sharp tips. J Vacuum Sci Technol B Microelectron Nanometer Struct 9(2):601

40. Ekvall I, Wahlström E, Claesson D, Olin H, Olsson E (1999) Preparation and characterization of electrochemically etched W tips for STM. Meas Sci Technol 10(1):11–18
41. Hagedorn T, El Ouali M, Paul W, Oliver D, Miyahara Y, Grütter PH (2011) Refined tip preparation by electrochemical etching and ultrahigh vacuum treatment to obtain atomically sharp tips for scanning tunneling microscope and atomic force microscope. Rev Sci Instrum 82(11):113903
42. Lucier A-S (2004) Preparation and characterization of tungsten tips suitable for molecular electronics studies. Master's thesis, McGill University
43. Setvin M, Javorský J, Turcinková D, Matolinová I, Sobotik P, Kocán P, Ošt'ádal I (2012) Ultrasharp tungsten tips-characterization and nondestructive cleaning. Ultramicroscopy 113:152–157
44. Greiner M, Kruse P (2007) Recrystallization of tungsten wire for fabrication of sharp and stable nanoprobe and field-emitter tips. Rev Sci Instrum 78(2):026104
45. Verlinden B, Driver J, Samajdar I, Doherty RD (2007) Thermo-mechanical processing of metallic materials. Elsevier, Oxford
46. Webber RD, Walls JM, Smith R (1978) Ring counting in field-ion micrographs. J Microsc 113(3):291–299
47. Bolin PL, Ranganathan BN, Bayuzick RJ (1976) Determination of field ion tip shapes. J Phys E Sci Instrum 9(5):363–365
48. Webber RD, Walls JM (1979) The shape of field-ion emitters. J Phys D Appl Phys 12(9):1589–159
49. Moore AJW (1962) The structure of atomically smooth spherical surfaces. J Phys Chem Solid 23(7):907–912
50. Rao PVM, Jensen CP, Silver RM (2004) Enhanced model for scanning tunneling microscope tip geometry measured with field ion microscopy. J Vacuum Sci Technol B Microelectron Nanometer Struct 22(2):636–641
51. Falter J, Langewisch G, Hölscher H, Fuchs H, Schirmeisen A (2013) Field ion microscopy characterized tips in noncontact atomic force microscopy: quantification of long-range force interactions. Phys Rev B 87(11):115412
52. Urban R, Wolkow RA, Pitters JL (2012) Field ion microscope evaluation of tungsten nanotip shape using He and Ne imaging gases. Ultramicroscopy 122:60–64
53. Pitters JL, Urban R, Wolkow R (2012) Creation and recovery of a W(111) single atom gas field ion source. J Chem Phys 136(15):154704
54. Rezeq M, Pitters J, Wolkow R (2006) Tungsten nanotip fabrication by spatially controlled field-assisted reaction with nitrogen. J Chem Phys 124(20):204716
55. Rezeq M, Pitters J, Wolkow R (2008) Nano-tip fabrication by spatially controlled etching. US Patent 7431856 B2, Dec 2008
56. Ehrlich G, Hudda FG (1962) Direct observation of individual adatoms: nitrogen on tungsten. J Chem Phys 36(12):3233
57. Mulson JF, Müller EW (1963) Corrosion of tungsten and iridium by field desorption of nitrogen and carbon monoxide. J Chem Phys 38(11):2615
58. Ermanoski I, Pelhos K, Chen W, Quinton JS, Madey TE (2004) Oxygen-induced nano-faceting of Ir(210). Surf Sci 549(1):1–23
59. Song K-J, Dong C-Z, Madey TE (1991) Faceting of W (111) induced by Ultrathin Pd films. Langmuir 6:3019–3026
60. Szczepkowicz A, Ciszewski A, Bryl R, Oleksy C, Nien C-H, Wu Q, Madey TE (2005) A comparison of adsorbate-induced faceting on flat and curved crystal surfaces. Surf Sci 599(1–3):55–68
61. Chang C-C, Kuo H-S, Tsong TT, Hwang I-S (2009) A fully coherent electron beam from a noble-metal covered W(111) single-atom emitter. Nanotechnology 20(11):115401
62. Fu T-Y, Lin Y-C, Kuo H-S, Hwang I-S, Tsong TT (2007) Study of two types of Ir or Rh covered single atom pyramidal W tips. Surf Sci 601(18):3992–3995

63. Hwang I-S, Kuo H-S, Chang C-C, Tsong TT (2010) Noble-metal covered W(111) single-atom electron sources. J Electrochem Soc 157(2):7
64. Kuo H-S, Hwang I-S, Fu T-Y, Hwang Y-S, Lu Y-H, Lin C-Y, Tsong TT, Hou J-L (2009) A single-atom sharp iridium tip as an emitter of gas field ion sources. Nanotechnology 20(33):335701
65. Kuo H-S, Hwang I-S, Fu T-Y, Lin Y-C, Chang C-C, Tsong TT (2006) Noble Metal/W(111) single-atom tips and their field electron and ion emission characteristics. Jpn J Appl Phys 45(11):8972–8983
66. Kuo H-S, Hwang I-S, Fu T-Y, Lin Y-C, Chang C-C, Tsong TT (2006) Preparation of single-atom tips and their field emission behaviors. e-J Surf Sci Nanotechnol 4(February):233–238
67. Kuo H-S, Hwang I-S, Fu T-Y, Lu Y-H, Lin C-Y, Tsong TT (2008) Gas field ion source from an Ir/W <111> single-atom tip. Appl Phys Lett 92(6):063106
68. Nomura K, Rokuta E, Itagaki T, Oshima C, Kuo H-S, Tsong TT (2008) Electron emission characteristics of Au-covered tungsten <111> Nanotips. e-J Surf Sci Nanotechnol 6(January):25–28
69. Golubok A, Masalov S, Tarasov N (1992) Thermofield tip formation in UHV/STM combined with field-emission microscope. Ultramicroscopy 42–44:1574–1579
70. Pavlov VG (2005) Field-desorption microscopy study of the deformation of a tungsten tip subjected to thermal treatment in an electric field. Phys Solid State 47(11):2180
71. Pavlov VG (2006) Variations in shapes of outgrowths on a tungsten tip during growth in an electric field. Phys Solid State 48(5):969–972
72. Pavlov VG (2007) Atomically sharp <111> trihedral angle of a tungsten tip. Phys Solid State 49(8):1579–1582
73. Fischer-Cripps AC (2011) Nanoindentation, volume 1 of mechanical engineering series. Springer, New York
74. Ehrlich G, Hudda FG (1960) Observation of adsorption on an atomic scale. J Chem Phys 33(4):1253
75. Holscher AA, Sachtler WMH (1966) Chemisorption and surface corrosion in the tungsten + carbon monoxide system, as studied by field emission and field ion microscopy. Discuss Faraday Soc 41:29
76. Cranstoun GKL, Anderson JS (1972) Field ion microscope studies of very low coverage low temperature oxygen adsorption on tungsten. Surf Sci 32(2):397–421
77. Ehrlich G, Hudda FG (1963) Promoted field desorption and the visibility of adsorbed atoms in the ion microscope. Philos Mag 8(93):1587–1591
78. Lewis RT, Gomer R (1971) Adsorption studies in the field ion microscope with argon imaging. Surf Sci 26(1):197–229
79. Müller EW, Tsong TT (1974) Field ion microscopy, field ionization and field evaporation. Prog Surf Sci 4(i):1–139
80. Paul W, Miyahara Y, Grütter PH (2012) Implementation of atomically defined field ion microscopy tips in scanning probe microscopy. Nanotechnology 23(33):335702
81. Müller EW (1957) Study of atomic structure of metal surfaces in the field ion microscope. J Appl Phys 28(1):1
82. Lias SG (2011) Ionization energies of gas-phase molecules. In: CRC Handbook of chemistry and physics, 92nd edn. CRC Press, Boca Raton
83. Singleton JH (2001) Practical guide to the use of Bayard-Alpert ionization gauges. J Vacuum Sci Technol A Vacuum Surf Films 19(4):1712
84. Weston GF (1985) Ultrahigh vacuum practice. Butterworth, Toronto
85. Zelterman D (2006) Models for discrete data. Oxford University Press, New York
86. Paul W, Miyahara Y, Grütter PH (2013) Simple Si(111) surface preparation by thin wafer cleavage. J Vacuum Sci Technol A Vacuum Surf Films 31(2):023201
87. Kuk Y, Silverman PJ (1986) Role of tip structure in scanning tunneling microscopy. Appl Phys Lett 48(23):1597

88. Kuk Y, Silverman PJ (1989) Scanning tunneling microscope instrumentation. Rev Sci Instrum 60(2):165
89. Sakurai T, Hashizume T, Hasegawa Y, Kamiya I, Sano N, Yokoyama H, Tanaka H, Sumita I, Hyodo S (1990) New versatile room-temperature field ion scanning tunneling microscopy. J Vacuum Sci Technol A Vacuum Surf Films 8(1):324
90. Sakurai T, Hashizume T, Kamiya I, Hasegawa Y, Sano N, Pickering H, Sakai A (1990) Field ion-scanning tunneling microscopy. Prog Surf Sci 33(1):3–89
91. Hashizume T, Sakurai T (1997) FI-STM Investigation of fullerenes adsorbed on the semiconductor and metal surfaces (STM-C60), science reports of the research institutes, Tohoku University. Ser A Phy Chem Metall A44:17
92. Hashizume T, Wang X-D, Nishina Y, Shinohara H, Saito Y, Kuk Y, Sakurai T (1992) Field ion-scanning tunneling microscopy study of C 60 on the Si(100) surface. Jpn J Appl Phys 31(Part 2, No. 7A):L880–L883
93. Wang X-D, Hashizume T, Shinohara H, Saito Y, Nishina Y, Sakurai T (1992) Scanning tunneling microscopy of C 60 on the Si(111)7 × 7 surface. Jpn J Appl Phys 31(Part 2, No. 7B):L983–L986
94. Hashizume T, Sumita I, Murata Y, Hyodo S, Sakurai T (1991) Cs adsorption on the Si(100) 2 × 1 surfaces. J Vacuum Sci Technol B Microelectron Nanometer Struct 9(2):742
95. An T, Eguchi T, Akiyama K, Hasegawa Y (2005) Atomically-resolved imaging by frequency-modulation atomic force microscopy using a quartz length-extension resonator. Appl Phys Lett 87(13):133114
96. Tomitori M, Hirano N, Iwawaki F, Watanabe Y, Takayanagi T, Nishikawa O (1990) Elaboration and evaluation of tip manipulation of scanning tunneling microscopy. J Vacuum Sci Technol A Vacuum Surf Films 8(1):425
97. Tomitori M, Sugata K, Okuyama G, Kimata H (1996) Reproducibility of scanning tunneling spectroscopy of Si(111)7 × 7 using a build-up tip. Surf Sci 355(1–3):21–30
98. Spence JCH, Weierstall U, Lo W (1996) Atomic species identification in scanning tunneling microscopy by time-of-flight spectroscopy. J Vacuum Sci Technol B Microelectron Nanometer Struct 14(3):1587
99. Weierstall U, Spence JCH (1998) Atomic species identification in STM using an imaging atom-probe technique. Surf Sci 398(1–2):267–279
100. Fian A, Ernst C, Leisch M (1999) Combined atom probe and STM study of tip-substrate interactions. Fresenius J Anal Chem 365(1–3):38–42
101. Landman U, Luedtke WD, Burnham NA, Colton RJ (1990) Atomistic mechanisms and dynamics of adhesion, nanoindentation, and fracture. Science 248(4954):454–461
102. Nishikawa O, Walko R (1971) Field ion microscopical observation of twinning in iridium induced by a mechanical contact. Acta Metall 19(11):1163–1168
103. Fian A, Leisch M (2003) Study on tip-substrate interactions by STM and APFIM. Ultramicroscopy 95(1–4):189–197
104. Paul W, Oliver D, Miyahara Y, Grütter P (2014) FIM tips in SPM: Apex orientation and temperature considerations on atom transfer and diffusion. Appl Surf Sci 305:124–132
105. Schirmeisen A, Cross G, Stalder A, Grütter PH, Dürig U (2000) Metallic adhesion forces and tunneling between atomically defined tip and sample. Appl Surf Sci 157(4):274–279
106. An T, Nishio T, Eguchi T, Ono M, Nomura A, Akiyama K, Hasegawa Y (2008) Atomically resolved imaging by low-temperature frequency-modulation atomic force microscopy using a quartz length- extension resonator. Rev Sci Instrum 79(3):033703
107. Hudlet S, Saint JM, Guthmann C, Berger J (1998) Evaluation of the capacitive force between an atomic force microscopy tip and a metallic surface. Eur Phys J B 2(1):5–10
108. Argento C, French RH (1996) Parametric tip model and force-distance relation for Hamaker constant determination from atomic force microscopy. J Appl Phys 80(11):6081
109. Sadewasser S, Jelinek P, Fang C-K, Custance O, Yamada Y, Sugimoto Y, Abe M, Morita S (2009) New insights on atomic-resolution frequency-modulation kelvin-probe force-microscopy imaging of semiconductors. Phys Rev Lett 103:266103

110. Mohn F, Gross L, Moll N, Meyer G (2012) Imaging the charge distribution within a single molecule. Nat Nanotechnol 7(4):227–231
111. Sinnott SB, Heo S-J, Brenner DW, Harrison JA, Irving DL (2011) Computer simulations of nanometer-scale indentation and friction. In: Nanotribology and Nanomechanics I. Springer, Berlin/Heidelberg, chapter 10
112. Luan B, Robbins MO (2005) The breakdown of continuum models for mechanical contacts. Nature 435(7044):929–932
113. Lassner E, Schubert W-D (1999) Tungsten. Springer US, New York (DOI: 10.1007/978-1-4615-4907-9)
114. Cross GLW, Schirmeisen A, Grütter PH, Dürig U (2006) Plasticity, healing and shakedown in sharp- asperity nanoindentation. Nat Mater 5(5):370–376
115. Oliver DJ, Maassen J, El Ouali M, Paul W, Hagedorn T, Miyahara Y, Qi Y, Guo H, Grütter PH (2012) Conductivity of an atomically defined metallic interface. Proc Natl Acad Sci U S A 109(47):19097–19102
116. Paul W, Oliver D, Miyahara Y, Grütter PH (2013) Minimum threshold for incipient plasticity in the atomic-scale nanoindentation of Au(111). Phys Rev Lett 110(13):135506
117. Paul W, Oliver D, Miyahara Y, Grütter P (2013) Transient adhesion and conductance phenomena in initial nanoscale mechanical contacts between dissimilar metals. Nanotechnology 24(47):475704
118. Oliver D, Paul W, El Ouali M, Hagedorn T, Miyahara Y, Qi Y, Grütter P (2014) One-to-one spatially matched experiment and atomistic simulations of nanometre-scale indentation. Nanotechnology 25:025701
119. Lawn BR, Cook RF (2012) Probing material properties with sharp indenters: a retrospective. J Mater Sci 47(1):1–22
120. Agraït N, Yeyati AL, van Ruitenbeek JM (2003) Quantum properties of atomic-sized conductors. Phy Rep 377(2–3):81–279
121. Feldman B, Park S, Haverty M, Shankar S, Dunham ST (2010) Simulation of grain boundary effects on electronic transport in metals, and detailed causes of scattering. Phys Status Solidi (B) 247(7):1791–1796
122. Srivastava MK, Wang Y, Zhang X-G, Nicholson DMC, Cheng H-P (2012) Plane-wave transport method for low-symmetry lattices and its application. Phys Rev B 86(7):075134
123. Zhou B-H, Xu Y, Wang S, Zhou G, Xia K (2010) An ab initio investigation on boundary resistance for metallic grains. Solid State Commun 150(29–30):1422–1424
124. Xu P, Xia K, Zwierzycki M, Talanana M, Kelly P (2006) Orientation-dependent transparency of metallic interfaces. Phys Rev Lett 96(17):176602
125. Kim T-H, Zhang X-G, Nicholson DM, Evans BM, Kulkarni NS, Radhakrishnan B, Kenik EA, Li A-P (2010) Large discrete resistance jump at grain boundary in copper nanowire. Nano Lett 10(8):3096–3100
126. Clark KW, Zhang X-G, Vlassiouk IV, He G, Feenstra RM, Li A-P (2013) Spatially resolved mapping of electrical conductivity across individual domain (Grain) boundaries in graphene. ACS Nano 9:7956–7966